iScience

CellPress

Article

Efficient Deep-Blue Electrofluorescence with an External Quantum Efficiency Beyond 10%

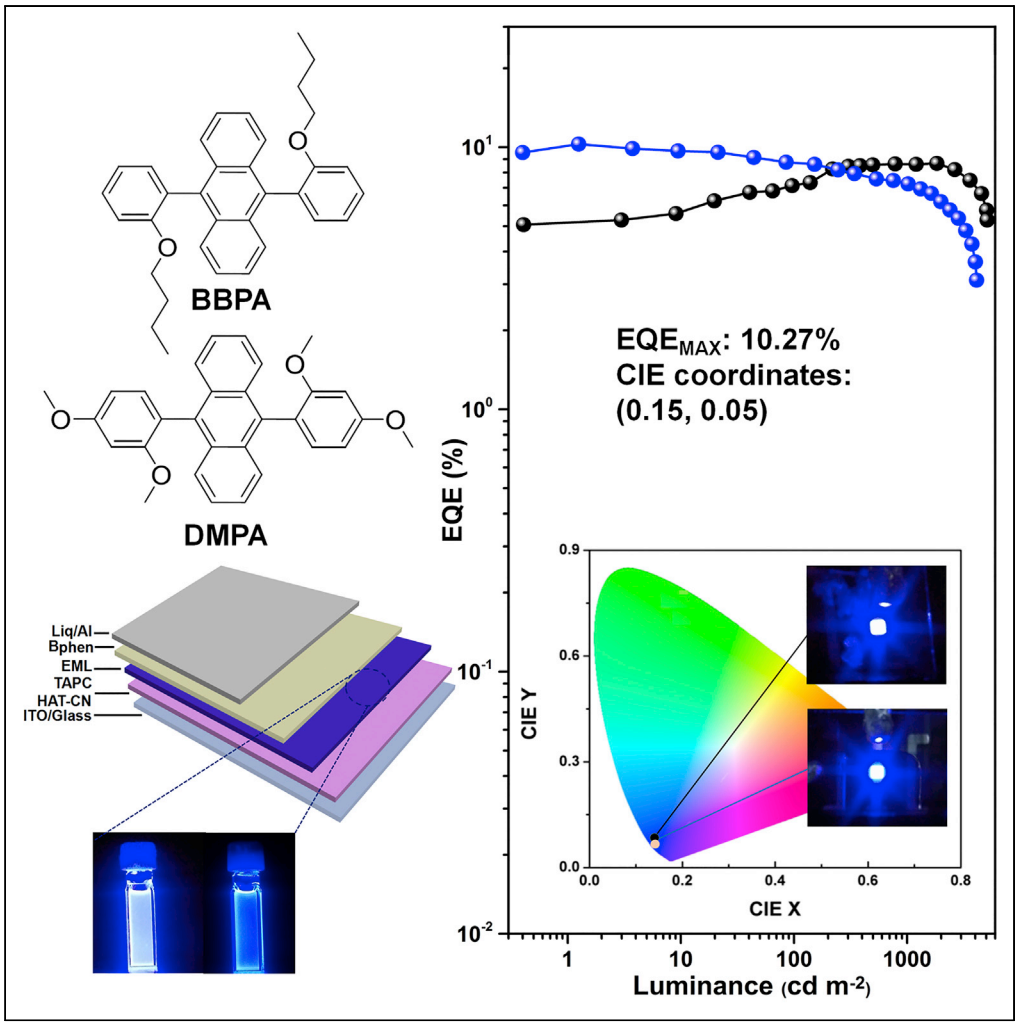

Shuanglong Wang, Mengya Qiao, Zhonghua Ye, ..., Chunju Li, Bin Wei, Wai-Yeung Wong

cjli@shu.edu.cn (C.L.)
bwei@shu.edu.cn (B.W.)
wai-yeung.wong@polyu.edu.hk (W.-Y.W.)

HIGHLIGHTS

Highly efficient deep-blue luminogens BBPA and DMPA are synthesized

Low-efficiency roll-off deep-blue OLEDs with CIE coordinate Y < 0.06

Record-high external quantum efficiency of 10.27% for deep-blue fluorescent OLEDs

Host matrix of twisted structure showing steric effect reduces intermolecular aggregation

Wang et al., iScience 9, 532–541
November 30, 2018 © 2018 The Authors.
https://doi.org/10.1016/j.isci.2018.10.026

iScience

CellPress

Article

Efficient Deep-Blue Electrofluorescence with an External Quantum Efficiency Beyond 10%

Shuanglong Wang,[1,6] Mengya Qiao,[2,6] Zhonghua Ye,[3] Dehai Dou,[1] Minyu Chen,[1] Yan Peng,[1] Ying Shi,[3] Xuyong Yang,[1] Lei Cui,[2] Jiuyan Li,[4] Chunju Li,[2,*] Bin Wei,[1,*] and Wai-Yeung Wong[5,7,*]

SUMMARY

The design of blue fluorescent materials combining both deep-blue emission (CIE_y<0.06) and high-efficiency climbing over the typically limited exciton production efficiency of 25% is a challenge for organic light-emitting diodes (OLEDs). In this work, we have synthesized two blue luminogens, *trans*-9,10-bis(2-butoxyphenyl)anthracene (BBPA) and *trans*-9,10-bis (2,4-dimethoxyphenyl)anthracene with high photoluminescence quantum yields (PLQYs) of 89.5% and 87.0%, respectively. Intriguingly, we have proposed a strategy to avoid aggregation-caused quenching, which can effectively reduce the undesirable excimeric emission by introducing two host matrices with twisted molecular structure, 9,10-di(naphth-2-yl) anthracene and 10,10′-bis-(4-fluorophenyl)-3,3′-dimethyl-9,9′-bianthracene (MBAn-(4)-F), in the BBPA emission layer. The device containing the EML of BBPA-doped MBAn-(4)-F exhibited a high external quantum efficiency of 10.27% for deep-blue emission with the Commission International de L'Eclairage CIE coordinates of (0.15, 0.05) via the steric effect. Importantly, this represents an advance in deep-blue-emitting fluorescent OLED architectures and materials that meet the requirements of high-definition display.

INTRODUCTION

New-generation organic light-emitting diodes (OLEDs) are promising candidates for future displays and solid-state lighting applications owing to their unique cost-effective, lightweight, and flexibility features (Kee et al., 2018; Zhang et al., 2017; Pan et al., 2017; Lian et al., 2018). More importantly, high-performance deep-blue materials, which have a Commission International de L'Eclairage (CIE) coordinate of CIE_y< 0.10 and even match the blue standard with the CIE (x, y) coordinates at (0.15, 0.06) of European Broadcasting Union, can provide widened color gamut, which is crucial to full-color displays (Wu et al., 2013; Tang et al., 2015; Tao et al., 2017; Wada et al., 2018). Hence, it is of great significance to develop deep-blue-emitting materials capable of achieving high efficiency and color saturation simultaneously for OLEDs (Liu et al., 2014; Cai et al., 2016; Lee et al., 2017; Shao et al., 2017).

To achieve maximum external quantum efficiency (EQE), the highest priority is to harvest triplet energy to break the internal quantum efficiency (IQE) limit of 25% for singlet spin states (Luo and Aziz, 2010). As the representative molecular frameworks, phosphorescent materials are extensively investigated because 100% IQE can be obtained (Lee et al., 2013). However, the phosphorescent materials containing non-renewable and unevenly distributed heavy metal elements such as Ir, Au, or Pt and the strong quenching effect of the long-lived triplet excitons at high luminescence hinders the commercialization of phosphorescent OLEDs (Tao et al., 2011; Zhang et al., 2016; Kim et al., 2018). On the other hand, although the use of metal-free thermally activated delayed fluorescence (TADF) materials via a reverse intersystem crossing (RISC) has been considered as a promising strategy and important breakthrough for the realization of highly efficient third-generation OLEDs, it still remains difficult to develop highly efficient deep blue materials with a suitably wide band gap (Hirata et al., 2015; Zhang et al., 2014; Hatakeyama et al., 2016). Moreover, the slow RISC process between the lowest triplet excited state (T_1) and the lowest singlet excited state (S_1) of TADF materials leads to the accumulation of triplet excitons at high luminance. Thus, even with lower electroluminescence (EL) efficiencies, considerable attention is still directed toward fully organic fluorophores such as carbazole (Lin et al., 2009; Li et al., 2015), imidazole (Li et al., 2016; Chen et al., 2017a), pyrene (Wu et al., 2010; Tao et al., 2010), fluorene

[1]School of Mechatronic Engineering and Automation, Key Laboratory of Advanced Display and System Applications, Ministry of Education, Shanghai University, 149 Yanchang Road, Shanghai, 200072, P. R. China

[2]Department of Chemistry, Center for Supramolecular Chemistry and Catalysis, Shanghai University, 99 Shangda Road, Shanghai 200444, P. R. China

[3]School of Materials Science and Engineering, Shanghai University, Shanghai 200444, P. R. China

[4]School of Chemical Engineering, Dalian University of Technology, Liaoning 116024, P.R. China

[5]Institute of Molecular Functional Materials and Department of Applied Biology and Chemical Technology, Hong Kong Polytechnic University, Hung Hom, Kowloon, Hong Kong, P. R. China

[6]These authors contributed equally

[7]Lead Contact

*Correspondence: cjli@shu.edu.cn (C.L.), bwei@shu.edu.cn (B.W.), wai-yeung.wong@polyu.edu.hk (W.-Y.W.)

https://doi.org/10.1016/j.isci.2018.10.026

This is an open access article under the CC BY-NC-ND license (http://creativecommons.org/licenses/by-nc-nd/4.0/).

(Wu et al., 2004; Gao et al., 2010), anthracene, and their derivatives (Wu et al., 2014; Zambianchi et al., 2016; Li et al., 2017a).

Among the variety of deep-blue fluorescent materials, anthracene and its derivatives are considered to be the most promising deep-blue emitters due to their high photoluminescence (PL) quantum yield, tunability of properties by the modification of molecular structure, and high thermal stabilities (Danel et al., 2002; Kim et al., 2008). Using 9,10-di(naphth-2-yl)anthracene (ADN) and its tertiary butyl derivative, 2-*t*-butyl-9,10-di-(2-naphthyl) anthracene as emitters, Tang et al. reported blue emissions with good chromaticity and luminance efficiency of 3.5 cd A^{-1} corresponding to the CIE coordinates of (0.15, 0.23) and a half-life-time of 4,000 hr with an initial light output of 700 cd m^{-2} (Shi and Tang, 2002). Tang et al. reported an efficient blue-emitting molecule PIAnCN (phenanthroimidazole-anthracene derivative) consisting of cyano-substituted anthracene, and the PIAnCN-based nondoped OLEDs displayed a maximum EQE of 9.44% with CIE coordinates of (0.14, 0.19) (Tang et al., 2018). Recently, new mechanisms by utilizing triplet excitons, such as locally excited (LE) state, charge transfer (CT) state, and triplet-triplet annihilation (TTA), were developed to increase the IQE for fluorescent emitters in blue OLED applications. For example, by employing D-π-A-based phenanthro[9,10-*d*]imidazole (PI) carbazole hybrid fluorophores 1-(4-(*tert*-butyl)phenyl)-2-(4-(4-(9-phenyl-9*H*-carbazol-3-yl)naphthalen-1-yl)phenyl)- 1*H*-phenanthro[9,10-*d*]imidazole (TPINCz) with remarkable hybridized local charge transfer (HLCT) excited states as an emissive dopant, Chen et al. obtained a violet blue emission with CIE coordinates of (0.153, 0.059) and a record high EQE of 6.56% ± 0.11% at a brightness of 1,000 cd m^{-2} (Chen et al., 2017b). In addition, Li et al. synthesized a series of materials 2-(2′-hydroxyphenyl)oxazoles possessing an HLCT excited state, and the doped device reached a high EQE of 7.10% and an excellent color purity with the CIE coordinates of (0.15, 0.08) (Li et al., 2017b). From this viewpoint, the LE state, as an efficient way to use RISC arising from its larger transition moment with a larger orbital overlap, can provide a high radiative transition rate that is related to a high PL efficiency.

In this study, we have synthesized two deep-blue fluorescent emitters *trans*-9,10-bis(2-butoxyphenyl) anthracene (BBPA) and *trans*-9,10-bis (2,4-dimethoxyphenyl)anthracene (DMPA) based on 9,10-dibromoanthracene derivatives. These two molecules showed high photoluminescence quantum yields (PLQYs), deep-blue emission, and LE states, which make them suitable for efficient blue OLEDs. The nondoped device bearing BBPA and DMPA exhibited a maximum EQE of 5.7% and 4.46%, respectively. To avoid a lower energy state formation of excimer, we blended the synthesized luminogens into an appropriate host 1,3-bis(*N*-carbazolyl)benzene (mCP), ADN and 10,10′-bis-(4-fluorophenyl)-3,3′-dimethyl-9,9′-bianthracene (MBAn-(4)-F), respectively. Using BBPA- and DMPA-doped mCP (5.0 wt%) as the emission layer (EML), we have achieved efficient deep-blue OLEDs with maximum EQEs of 6.02% and 8.05% at the corresponding CIE coordinates of (0.15, 0.03) and (0.15, 0.05), respectively. Furthermore, we have found that the use of host matrices with twisted geometric molecular configuration, ADN and MBAn-(4)-F in BBPA emission layer, could significantly improve the intercoupling of blue OLEDs. The device containing the EML of BBPA-doped MBAn-(4)-F exhibited an unprecedentedly high EQE of 10.27% and deep-blue emission with the CIE coordinates of (0.15, 0.05) via the steric effect.

RESULTS AND DISCUSSION

Material Synthesis and Characterization

The synthetic routes for the two anthracene-based blue-emitting compounds are shown in Figure 1A. DMPA and BBPA can be synthesized through a one-pot Suzuki cross-coupling reaction from 9,10-dibromoanthracene and the corresponding boronic acid derivatives, with tetrakis(triphenylphosphine)palladium as the catalyst. They were purified by column chromatography on silica gel with dichloromethane and petroleum ether as the eluents. The two products were characterized by ^{1}H and ^{13}C NMR spectroscopy (Figures S1–S4) and high-resolution mass spectrometry. In addition, the structure of BBPA was also confirmed by single-crystal X-ray diffraction analysis (Figure 1C and Table S1).

To further reveal the electronic structures and excited state properties of these molecules, density functional theory (DFT) and time-dependent DFT calculations at the B3LYP level of theory using the basis set 6-31G(d) were performed. The frontier orbital distributions of this molecule between the highest occupied molecular orbital (HOMO) and the lowest unoccupied molecular orbital (LUMO) levels are shown in Figure 1B, and the data are summarized in Table S2. The HOMO and LUMO levels of BBPA and DMPA have similar distributions, being predominantly distributed over the central anthracene core. The energy

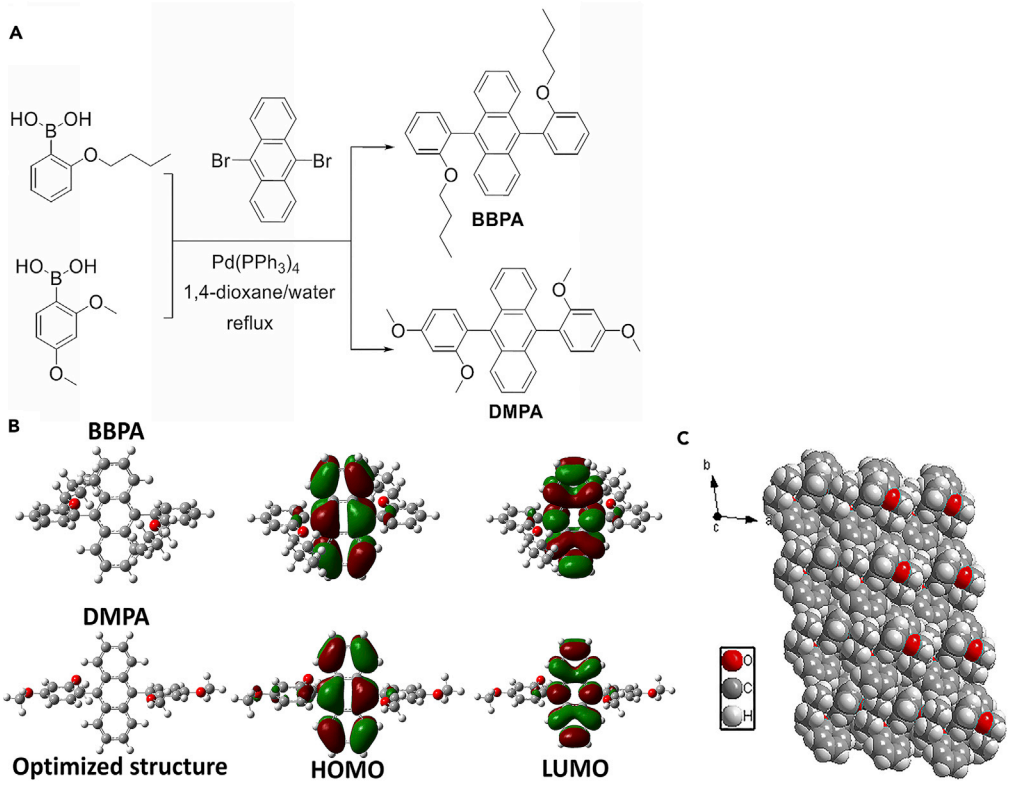

Figure 1. Molecular Structure Characteristics

(A) Synthetic approach to BBPA and DMPA.

(B) Molecular structures for BBPA and DMPA optimized at the B3LYP/6-1G(d) level of theory using Gaussian 09.

(C) Crystal packing of BBPA molecules.

Also see Figures S1–S4 and Table S1 and Data S1.

levels of the HOMO and LUMO were calculated to be in the range -(4.86–4.87) and -(1.37–1.41) eV, respectively, resulting in a wide energy gap of about 3.50 and 3.45 eV.

Photophysical and Thermal Properties

Figure 2A shows the ultraviolet-visible absorption and PL spectra of nondoped solid film of BBPA and DMPA. The spectra in CH_2Cl_2 solution of the two molecules are shown in Figure S5. The key data are

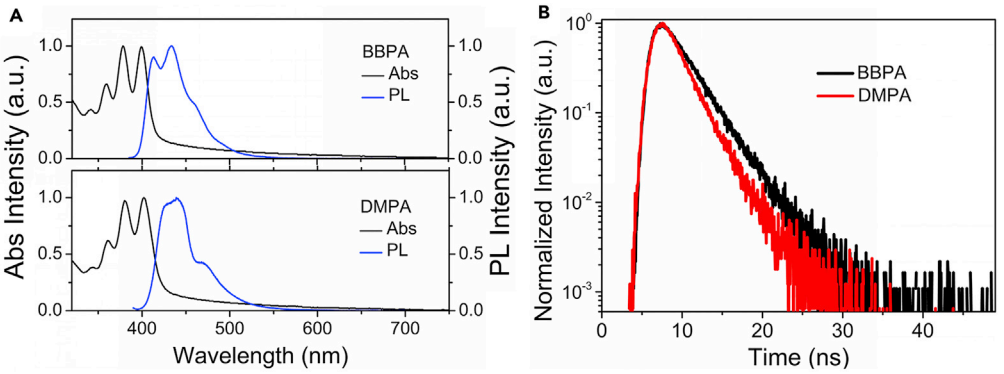

Figure 2. Photophysical Characteristics of BBPA and DMPA

(A) Absorption (black line) and fluorescent (blue line) spectra of BBPA and DMPA.

(B) The corresponding PL decay spectra in solid film at ambient condition.

Also see Figures S5 and S6, and Table S2.

Compound	T_d[a]/T_m[b] (°C)	λ_{abs}, max[c] (nm)	λ_{PL}, max[d] (nm)	PLQY[e] (%)	HOMO/LUMO[f] (eV)
BBPA	257/498	399/378/360/341	432	89.5	−5.81/−2.63
DMPA	309/339	402/380/361/341	438	87.0	−5.78/−2.48

Table 1. Summary of Thermal and Photophysical Properties of BBPA and DMPA

Also see Figures S7 and S8.

[a]Decomposition temperature.

[b]Melting point.

[c]Absorption maximum.

[d]Fluorescence emission peak in nondoped thin film.

[e]Absolute PL quantum yield evaluated by integrating sphere of nondoped film.

[f]Determined from the onset of photoelectron spectroscopy in the air, and the equation LUMO = HOMO + E_g.

summarized in Table 1. The fluorescence spectra of the nondoped films exhibited maximum emission bands at 433 and 439 nm with a relatively narrow full width at half-maximum (FWHM) of 54 nm and 42 nm, respectively, for BBPA and DPMA. As displayed in Figure 2B, the BBPA and DMPA in nondoped solid films showed monoexponential decay with lifetime (τ_s) of 3.13 and 2.48 ns, respectively. No delayed component can be observed, indicating that the emission exclusively originates from the prompt decay of the S_1 state (Figure S6).

The thermal stability of the emitters was determined by measurement of their glass transition temperature (T_g), decomposition temperature (T_d), and melting point (T_m) using differential scanning calorimetry and thermal gravimetric analysis under a nitrogen atmosphere. Both BBPA and DMPA have shown excellent thermal stability for organic electronics with T_d at 257°C and 309°C, respectively (in Figure S7), The photophysical and thermal properties of these two molecules are summarized in Table 1.

Photoelectron yield spectroscopy was employed to measure the practical HOMO levels of the two emitters in the neat thin films (Figure S8). The LUMO level was then determined by adding the corresponding HOMO level and the energy gap (E_g). As listed in Table 1, the HOMO and LUMO levels are estimated to be −5.81 and −2.63 eV for BBPA and −5.78 and −2.48 eV for DMPA, respectively.

Electroluminescence Performance

To evaluate the EL performance of the two materials as emitting cores, we initially fabricated two nondoped OLEDs (devices A0 and B0) with a structure of ITO/HAT-CN (5 nm)/TAPC (40 nm)/EML (20 nm)/Bphen (30 nm)/Liq (1 nm)/Al (150 nm). All the material structures are displayed in Figure S9, and the details of the device fabrication are given in the Methods. The device structures and the electroluminescent properties are shown in Figure 3 and summarized in Table 2.

The BBPA- and DMPA-based OLEDs display the highest EQE of 5.28% and 4.97% and deep-blue EL emission with CIE coordinates of (0.15, 0.06) and (0.16, 0.08) (at 7 V), respectively. It is worth noting that the device A0 shows serious efficiency roll-off due to excimeric emission at higher working voltage than device B0, in which a high EQE of 4.22% is still maintained at a practical luminance of 1,000 cd m^{-2} (Figures 3E, S10, and S11). The devices A0 and B0 show an emission peak at 432 and 436 nm, respectively, which coincides with their nondoped PL spectrum. The EL spectra are comparable to the PL spectra of solid film, indicating that the EL is mainly from the emissive materials (Lukas et al., 2003).

We also fabricated and optimized doped devices (devices A1 and B1) to further improve the efficiency and color purity. The detailed description of device optimization is illustrated in the Supplemental Information. The best result was obtained from the device ITO/HAT-CN (5 nm)/TAPC (40 nm)/mCP: dopants (20 nm)/Bphen (30 nm)/Liq (1 nm)/Al (150 nm) where mCP is the host material (Figures 4A and 4B). The dopant level was optimized to avoid any spectral broadening from aggregation of the excimeric emission and excavate the EL potential of these compounds (3, 5, and 10 wt % of BBPA and DMPA in mCP, Figures S12 and S13 and Table S3). The EL spectra (Figure 4C) and CIE diagram (Figure 4D) of both devices showed deep-blue emission with peaks at 412 and 428 nm, corresponding to the coordinates of (0.15, 0.03) and (0.15, 0.05), respectively. The light-emitting photographs of devices A1 and B1 are displayed in the inset of Figure 4D. All the doped devices show obviously blue-shifted EL spectra compared with the corresponding nondoped devices. It is noteworthy that device A1 with BBPA as the dopant exhibited extraordinary deep blue emission

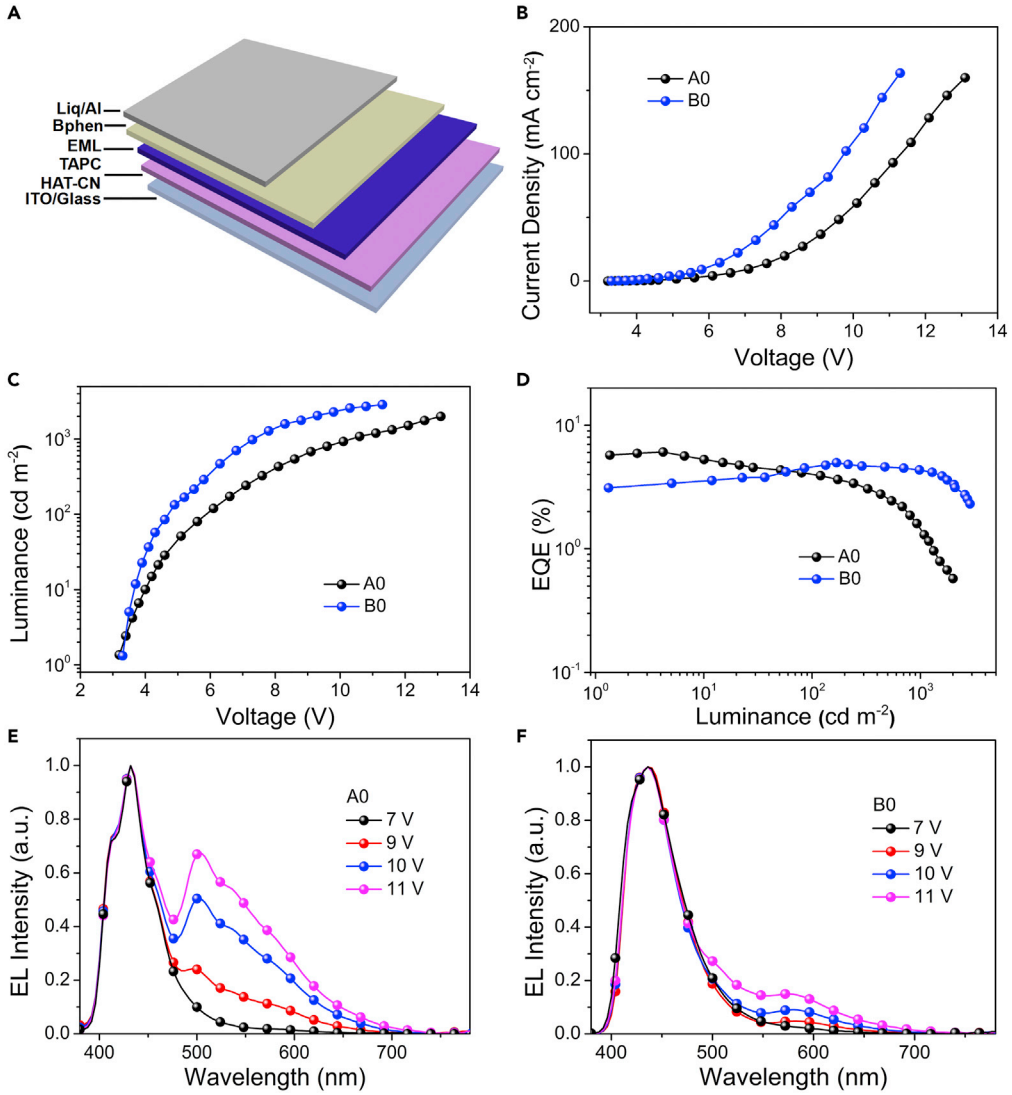

Figure 3. Performance of Nondoped Deep-Blue OLEDs Based on BBPA and DMPA Emitters.

(A) Device structures.

(B) Current density versus voltage characteristics.

(C) Luminance versus voltage characteristics.

(D–F) (D) External quantum efficiency versus luminance. (E and F) Electroluminescent spectra from BBPA and DMPA fluorescent OLEDs at different driving voltages.

Also see Figure S9.

with an FWHM of 43 nm and a high EQE value of 6.02%. The DMPA-based device B1 also showed excellent efficiency of 8.05% with an FWHM of 51 nm. To the best of our knowledge, the EQEs of devices A1 and B1 are the highest among the reported deep-blue devices with CIE_y<0.06 (Tang et al., 2018; Hu et al., 2014; Li et al., 2018). Furthermore, device B1 displayed an efficiency roll-up at low luminance and extremely low-efficiency roll-off at high luminance. For example, device B1 showed a maximum EQE of 8.05% (at 165 cd m^{-2}), although the EQE can still be maintained at 7.02% at 1,000 cd m^{-2}, corresponding to only 11.06% decrease compared with the maximum value. There are two possible reasons for the low-efficiency roll-off. First, excellent charge balance of the devices is achieved. It is well known that the charge balance is important for reducing the efficiency roll-off of an OLED device (Figure S14). The second reason is based on the use of doping blue emissive molecules into the mCP matrix, which can effectively remove the excimeric emission in the nondoped emitters (Figure 4C) resulting from the self-quenching of excitons (Lee et al., 2016).

Device[a]	Emitter	V_{on}[b] (V)	EL[c] (λ_{max})	CIE[d] (x, y)	FWHM[e] (nm)	EQE[f] (%)
						Max/100/1,000
A0	BBPA	3.2	432	0.15, 0.06	52	5.28/4.02/1.35
B0	DMPA	3.3	436	0.16, 0.08	62	4.97/4.61/4.22
A1	mCP:BBPA	3.5	412	0.15, 0.03	43	6.02/5.14/2.41
B1	mCP:DMPA	3.3	428	0.15, 0.05	51	8.05/8.02/7.16
A2	ADN:BBPA	3.3	432	0.15, 0.06	50	8.67/7.15/8.62
B2	ADN:DMPA	3.7	448	0.15, 0.09	68	4.84/4.58/4.62
A3	MBAn-(4)-F:BBPA	3.6	432	0.15, 0.05	51	10.27/8.70/7.25

Table 2. Summary of OLED Characteristics Using BBPA and DMPA as Dopants

Also see Figure S14, and Table S4.

[a]Device configuration: ITO/HAT-CN (5 nm)/TAPC (40 nm)/EML (20 nm)/Bphen (30 nm)/Liq (1 nm)/Al (100 nm).

[b]The operating voltage at a brightness of 1 cd m^{-2}.

[c]The EL emission wavelength at the maximum intensity.

[d]CIE 1931 coordinates at 7 V.

[e]FWHM of EL spectra.

[f]EQE at the maximum value/at 100 cd m^{-2}/at 1,000 cd m^{-2}.

Intriguingly, we found a novel host-guest system that can significantly improve the device performance by utilizing the steric effect. We employed highly steric molecules, ADN and MBAn-(4)-F as the host of BBPA in devices A2 and A3, and achieved an improved efficiency compared with planar-type mCP-based device (A1). As illustrated in Figure 5, devices A2 and A3 show the same emission peak at 432 nm and efficiencies of 8.67% and 10.27%, respectively. It is rational that the improved efficiency can be attributed to the employment of ADN and MBAn-(4)-F with twisted structure having stronger steric hindrance. Moreover, the use of highly steric host can largely reduce the concentration of excitons and thereby suppress intermolecular quenching effect in the solid state, and simultaneously improve the morphological stability that would resist crystallization and morphological transition-induced deterioration during the device operation (Figure S15) (Hung et al., 2017; Young et al., 2002). On the contrary, we found that device B2 using DMPA-doped ADN as an EML exhibited a decreased efficiency compared with device B1 with mCP as the host (Figure S16). The device B3 based on MBAn-(4)-F:5% DMPA emitter was also fabricated, and the key parameters are shown in Table S4. The EL spectra mainly originated from the ADN host emission (444 nm), which can be demonstrated from the consistent PL emission of the ADN molecule. Different emission mechanisms for the two doping systems can be ascribed to the following reasons. (1) The long chains in BBPA molecule facilitate energy transfer from ADN onto the guest molecule BBPA. (2) For the DMPA-doped ADN system, DMPA cannot effectively harvest the excitons without the long chains, leading to the generation of singlet excitons that are mainly formed in ADN.

We note that the efficiency of the device A3 employing MBAn-(4)-F:5% BBPA is significantly higher than that of the traditional fluorescent singlet exciton limit. This is among the best results of deep-blue fluorescent OLEDs with an EQE greater than 10% and CIE_y < 0.06. Nevertheless, Figure S17 displays a linear relationship between current density and EL intensity, and the transient EL decay of device A3 is shown in Figure S18, suggesting that TTA does not play a role (Pu et al., 2012). Furthermore, the transient PL spectrum reveals no delayed fluorescence. Nevertheless, the high EQE is in accordance with the LE state conducted by the natural transition orbital analysis and horizontal orientation of the emitting molecules, as shown in Figure S19. Out-coupling efficiency is also an uncertain parameter, and it is possible for the EQE to climb over 25% if the emitting molecules have a horizontal orientation when discussing the origin of high EQEs. The PLQY (ϕ) of the BBPA in neat film was measured to be 89.5%. The classical theoretical estimate for the maximum EQE of fluorescent OLEDs is considered by the equation: $EQE = \gamma \times \phi \times \chi_r \times \chi_{ext}$, where γ represents the charge balance factor (ideally equal to 1), χ_r represents the probability of formation of an emissive excited state in a recombination event, ϕ is the PLQY of the emissive material, and χ_{ext} is the out-coupling efficiency (Hung et al., 2017; Wu et al., 2018). Ideally, we assume that the out-coupling efficiency χ_{ext} should be 25%. Thus, the calculated χ_r is around 45.8%. This value is far superior to that of the conventional

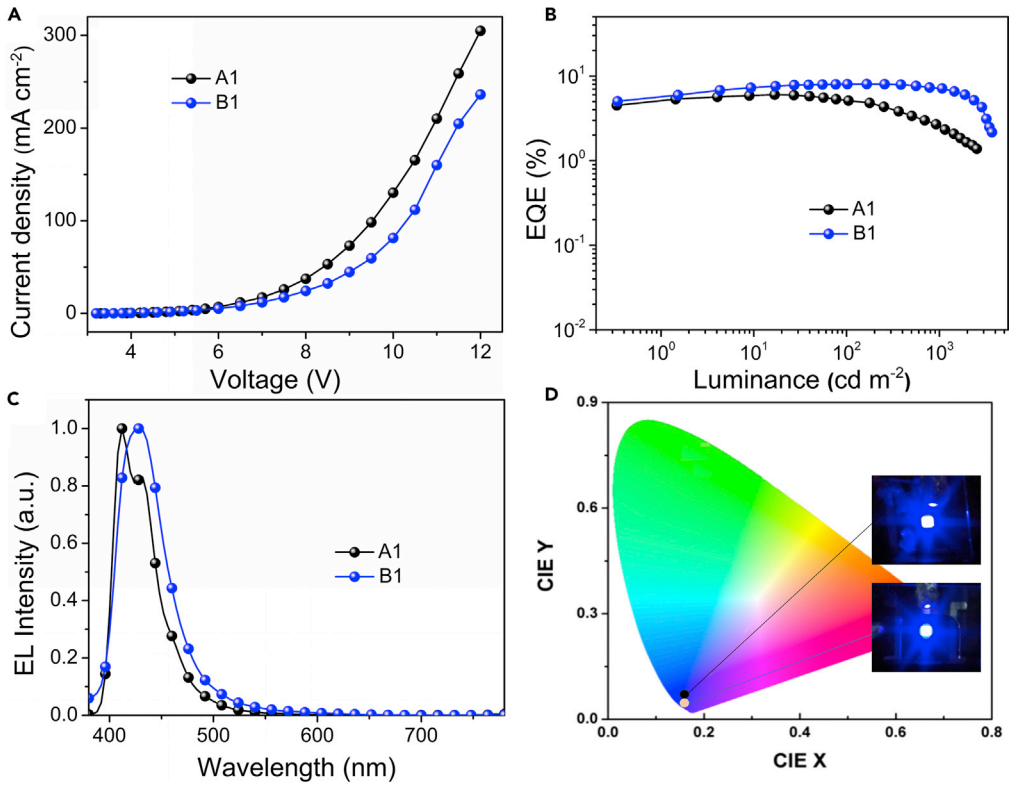

Figure 4. Performance of Optimized Deep-Blue OLEDs

(A) Current density versus voltage characteristics.

(B) External quantum efficiency versus luminance.

(C) Electroluminescent spectra.

(D) Comparison of the CIE coordinates of the EL spectra from two deep-blue fluorescent OLEDs.

Also see Figures S10–S13, and Table S3.

fluorescent materials ($ç_r$ = 25%). This result supports the fact that molecular orientation plays the key role in reaching high efficiency for the electrofluorescent devices. Finally, it is worth noting that the devices showing low-efficiency roll-off at high luminance are much desired for the practical full color display and lighting applications.

Conclusions

In conclusion, two efficient blue-emitting molecules BBPA and DMPA were designed and synthesized. The doped devices employing mCP as the host show a maximum EQE of 6.02% and 8.05% with a very-low-efficiency roll-off and deep-blue EL with CIE coordinates of (0.15, 0.03) and (0.15, 0.05), respectively. More importantly, we propose a facile and simple strategy of using steric effect to improve the EL performance for BBPA emitter. The introduction of ADN and MBAn-(4)-F with twisted structure having high steric hindrance to prevent intermolecular aggregation and reduce luminescence quenching is beneficial for increasing the device performance without shifting the emission peak. The resulting emitter employing ADN:5% BBPA and MBAn-(4)-F:5% BBPA displays deep-blue EL with CIE coordinates of (0.15, 0.06) and (0.15, 0.05), together with a high EQE of 8.67% and 10.27% and low roll-off at high brightness up to 1,000 cd m^{-2}, respectively. Our results represent state-of-the-art performance for deep-blue OLEDs, and we postulate that this work will open up a new way for highly efficient OLEDs with steric effect to develop deep-blue-emitting molecules.

Limitations of Study

The molecular orientation of the emitting layer is important to improve the efficiency of the organic light-emitting devices. Although the molecular orientation has been tested, it is still difficult to carry out the optical simulation of emitter due to the limitations of the scientific research conditions.

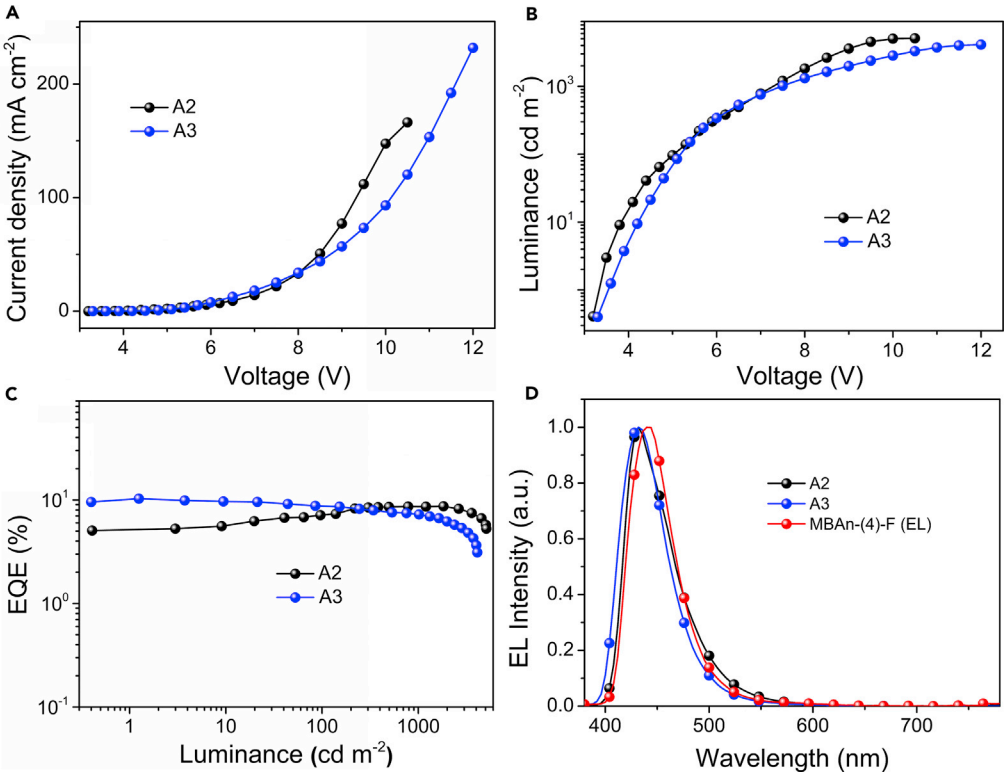

Figure 5. Performance of Optimized Deep-Blue OLEDs Based on Steric Effect

(A) Current density versus voltage characteristics.

(B) Luminance versus voltage characteristics.

(C) External quantum efficiency versus luminance.

(D) Electroluminescent spectra.

Also see Figures S15–S19.

METHODS

All methods can be found in the accompanying Transparent Methods supplemental file.

SUPPLEMENTAL INFORMATION

Supplemental Information includes Supplemental Experimental Procedures, 19 figures, 4 tables, and 1 data file and can be found with this article online at https://doi.org/10.1016/j.isci.2018.10.026.

ACKNOWLEDGMENTS

This work was financially supported by the Project of the National Science Foundation of China (grant Nos. 51725505, 61775130, and 21772118), "973" program (2015CB655005), the Science and Technology Committee of Shanghai (15590500500), and the Shanghai "Shuguang Program." W.-Y.W. thanks the Areas of Excellence Scheme of the University Grants Committee of HKSAR (AoE/P-03/08), the Hong Kong Polytechnic University (1-ZE1C), and the Endowment Fund from Ms. Clarea Au (847S) for financial support.

AUTHOR CONTRIBUTIONS

S. W. conceived the new idea and strategy, designed and fabricated the devices, and performed the measurements and analysis with assistance from Z.Y., D.D., M.C., Y.P., Y.S., and X.Y. M.Q and L.C. synthesized the deep-blue compounds and characterized their structures. B.W and W.-Y.W supervised this project and prepared the manuscript with assistance from the other co-authors J.L. and C.L. All authors have approved the final version of the manuscript.

DECLARATION OF INTERESTS

The authors declare no competing interests.

Received: July 6, 2018
Revised: September 30, 2018
Accepted: October 25, 2018
Published: November 30, 2018

REFERENCES

Cai, X., Gao, B., Li, X., Cao, Y., and Su, S.-J. (2016). Singlet-triplet splitting energy management via acceptor substitution: complanation molecular design for deep-blue thermally activated delayed fluorescence emitters and organic light-emitting diodes application. Adv. Funct. Mater. *26*, 8042–8052.

Chen, W.C., Yuan, Y., Xiong, Y., Rogach, A.L., Tong, Q.X., and Lee, C.S. (2017a). Aromatically C6- and C9-substituted phenanthro[9,10-d] imidazole blue fluorophores: structure-property relationship and electroluminescent application. ACS Appl. Mater. Interfaces *9*, 26268–26278.

Chen, W.C., Yuan, Y., Ni, S.F., Tong, Q.X., Wong, F.L., and Lee, C.S. (2017b). Achieving efficient violet-blue electroluminescence with CIE_y < 0.06 and EQE > 6% from naphthyl-linked phenanthroimidazole-carbazole hybrid fluorophores. Chem. Sci. *8*, 3599–3608.

Danel, K., Huang, T.-H., Lin, J.-T., Tao, Y.-T., and Chen, C.-H. (2002). Blue-emitting anthracenes with end-capping diarylamines. Chem. Mater. *14*, 3860–3865.

Gao, Z., Li, Z.., Xia, P., Wong, M., Cheah, K., and Chen, C. (2010). Efficient deep-blue organic light-emitting diodes: arylamine-substituted oligofluorenes. Adv. Funct. Mater. *17*, 3194–3199.

Hatakeyama, T., Shiren, K., Nakajima, K., Nomura, S., Nakatsuka, S., Kinoshita, K., Ni, J., Ono, Y., and Ikuta, T. (2016). Ultrapure blue thermally activated delayed fluorescence molecules: efficient HOMO-LUMO separation by the multiple resonance effect. Adv. Mater. *28*, 2777–2781.

Hirata, S., Sakai, Y., Masui, K., Tanaka, H., Lee, S.-Y., Nomura, H., Nakamura, N., Yasumatsu, M., Nakanotani, H., Zhang, Q., et al. (2015). Highly efficient blue electroluminescence based on thermally activated delayed fluorescence. Nat. Mater. *14*, 330–336.

Hu, J.-Y., Pu, Y.-J., Satoh, F., Kawata, S., Katagiri, H., Sasabe, H., and Kido, J. (2014). Bisanthracene-based donor-acceptor-type light-emitting dopants: highly efficient deep-blue emission in organic light-emitting devices. Adv. Funct. Mater. *24*, 2064–2071.

Hung, W.-Y., Wang, T.-C., Chiang, P.-Y., Peng, B.-J., and Wong, K.-T. (2017). Remote steric effect as a facile strategy for improving the efficiency of exciplex-based OLEDs. ACS Appl. Mater. Interfaces *9*, 7355–7361.

Kee, S., Kim, N., Park, B., Kim, B.-S., Hong, S., Lee, J.-H., Jeong, S., Kim, A., Jang, S.-Y., and Lee, K. (2018). Highly deformable and see-through polymer light-emitting diodes with all-conducting-polymer electrodes. Adv. Mater. *30*, 1703437.

Kim, S.-K., Yang, B., Ma, Y., Lee, J.-H., and Park, J.-W. (2008). Exceedingly efficient deep-blue electroluminescence from new anthracenes obtained using rational molecular design. J. Mater. Chem. *18*, 3376–3384.

Kim, S., Bae, H.-J., Park, S., Kim, W., Kim, J., and Kim, J.-S. (2018). Degradation of blue-phosphorescent organic light-emitting devices involves exciton-induced generation of polaron pair within emitting layers. Nat. Commun. *9*, 1211.

Lee, S., Kim, S.-O., Shin, H., Yun, H.-J., Yang, K., Kwon, S.-K., Kim, J.-J., and Kim, Y.-H. (2013). Deep-blue phosphorescence from perfluoro carbonyl-substituted iridium complexes. J. Am. Chem. Soc. *135*, 14321–14328.

Lee, J., Jung, H., Shin, H., Kim, J., Yokoyama, D., Nishimura, H., Wakamiya, A., and Park, J. (2016). Excimer emission based on control of molecular structure and intermolecular interactions. J. Mater. Chem. C *4*, 2784–2792.

Lee, H., Jo, M., Yang, G., Jung, H., Kang, S., and Park, J. (2017). Highly efficient dual anthracene core derivatives through optimizing side groups for blue emission. Dyes Pigm. *146*, 27–36.

Li, Y., Wang, Z., Li, X., Xie, G., Chen, D., Wang, Y.-F., Lo, C.-C., Lien, A., Peng, J., Cao, Y., and Su, S.-J. (2015). Highly efficient spiro[fluorene-9,9′-thioxanthene] core derived blue emitters and fluorescent/phosphorescent hybrid white organic light-emitting diodes. Chem. Mater. *27*, 1100–1109.

Li, C., Wei, J., Han, J., Li, Z., Song, X., and Zhang, Z. (2016). Efficient deep-blue OLEDs based on phenanthro[9,10-d]imidazole-containing emitters with AIE and bipolar transporting properties. J. Mater. Chem. C *4*, 10120–10129.

Li, C., Li, Z., Yan, X., Zhang, Y., Zhang, Z., and Wang, Y. (2017a). Structurally simple non-doped sky-blue OLEDs with high luminance and efficiencies at low driving voltages. J. Mater. Chem. C *5*, 1973–1980.

Li, B., Tang, G., Zhou, L., Wu, D., Lan, J., Zhou, L., and You, J. (2017b). Unexpected sole enol-form emission of 2-(2′-Hydroxyphenyl) oxazoles for highly efficient deep-blue-emitting organic electroluminescent devices. Adv. Funct. Mater. *27*, 1605245.

Li, J., Zhang, R., Wang, Z., Zhao, B., Xie, J., Zhang, F., Wang, H., and Guo, K. (2018). Zig-zag acridine/sulfone derivative with aggregation-induced emission and enhanced thermally activated delayed fluorescence in amorphous phase for highly efficient nondoped blue organic light-emitting diodes. Adv. Opt. Mater. *6*, 1701256.

Lian, H., Tang, Z., Guo, H., Zheng, Z., Wu, J., Dong, Q., Zhu, F., Wei, B., and Wong, W.-Y. (2018). Magnetic nanoparticles/PEDOT: PSS composite hole-injection layer for efficient organic light-emitting diodes. J. Mater. Chem. C *47*, 4854–4858.

Lin, S.-L., Chan, L.-H., Lee, R.-H., Yen, M.-Y., Kuo, W.J., Chen, C.-T., and Jeng, R.-J. (2009). Highly Efficient carbazole-p-dimesitylborane bipolar fluorophores for nondoped blue organic light-emitting diodes. Adv. Mater. *20*, 3947–3952.

Liu, C., Fu, Q., Zou, Y., Yang, C., Ma, D., and Qin, J. (2014). Low turn-on voltage, high-power-efficiency, solution-processed deep-blue organic light-emitting diodes based on starburst oligofluorenes with diphenylamine end-capper to enhance the HOMO level. Chem. Mater. *26*, 3074–3083.

Lukas, A.S., Bushard, P.J., Weiss, E.A., and Wasielewski, M.R. (2003). Mapping the influence of molecular structure on rates of electron transfer using direct measurements of the electron spin-spin exchange interaction. J. Am. Chem. Soc. *125*, 3921.

Luo, Y., and Aziz, H. (2010). Correlation between triplet-triplet annihilation and electroluminescence efficiency in doped fluorescent organic light-emitting devices. Adv. Funct. Mater. *20*, 1285–1293.

Pan, Y., Xia, Y., Zhang, H., Qiu, J., Zheng, Y., and Chen, Y. (2017). Recent advances in alternating current-driven organic light-emitting devices. Adv. Mater. *29*, 1701441.

Pu, Y.J., Nakata, G., Satoh, F., Sasabe, H., Yokoyama, D., and Kido, J. (2012). Optimizing the charge balance of fluorescent organic light-emitting devices to achieve high external quantum efficiency beyond the conventional upper limit. Adv. Mater. *24*, 1765–1770.

Shao, S., Hu, J., Wang, X., Wang, L., Jing, X., and Wang, F. (2017). Blue thermally activated delayed fluorescence polymers with nonconjugated backbone and through-space charge transfer effect. J. Am. Chem. Soc. *139*, 17739–17742.

Shi, J., and Tang, C.W. (2002). Anthracene derivatives for stable blue-emitting organic electroluminescence devices. Appl. Phys. Lett. *80*, 3201–3203.

Tang, X., Bai, Q., Peng, Q., Gao, Y., Li, J., Liu, Y., Yao, L., Lu, P., Yang, B., and Ma, Y. (2015). Efficient deep blue electroluminescence with an external quantum efficiency of 6.8% and CIE_y < 0.08 based on a phenanthroimidazole-sulfone hybrid donor-acceptor molecule. Chem. Mater. *27*, 7050–7057.

Tang, X., Bai, Q., Shan, T., Li, J., Gao, Y., Liu, F., Liu, H., Peng, Q., Yang, B., Li, F., and Lu, P. (2018). Efficient nondoped blue fluorescent organic

light-emitting diodes (OLEDs) with a high external quantum efficiency of 9.4% @ 1000 cd m^{-2} based on phenanthroimidazole-anthracene derivative. Adv. Funct. Mater. *28*, 1705813.

Tao, S., Zhou, Y., Lee, C.-S., Zhang, X., and Lee, S.-T. (2010). High-efficiency nondoped deep-blue-emitting organic electroluminescent device. Chem. Mater. *22*, 2138–2141.

Tao, Y., Yang, C., and Qin, J. (2011). Organic host materials for phosphorescent organic light-emitting diodes. Chem. Soc. Rev. *40*, 2943–2970.

Tao, P., Zhang, Y., Wang, J., Wei, L., Li, H., and Li, X. (2017). Highly efficient blue phosphorescent iridium(III) complexes with various ancillary ligands for partially solution-processed organic light-emitting diodes. J. Mater. Chem. C *5*, 9306–9314.

Wada, Y., Kubo, S., and Kaji, H. (2018). Adamantyl substitution strategy for realizing solution-processable thermally stable deep-blue thermally activated delayed fluorescence materials. Adv. Mater. *30*, 1705641.

Wu, C.-C., Lin, Y.-T., Wong, K.-T., Chen, R.-T., and Chien, Y.-Y. (2004). Efficient organic blue-light-emitting devices with double confinement on terfluorenes with ambipolar carrier transport properties. Adv. Mater. *16*, 61–65.

Wu, K.-C., Ku, P.-J., Lin, C.-S., Shi, H.-T., Wu, F.-I., Huang, M.-J., Lin, J.-J., Chen, I.-C., and Cheng, C.-H. (2010). The photophysical properties of dipyrenylbenzenes and their application as exceedingly efficient blue emitters for electroluminescent devices. Adv. Funct. Mater. *18*, 67–75.

Wu, S., Aonuma, M., Zhang, Q., Huang, S., Nakagawa, T., Kuwabara, K., and Adachi, C. (2013). High-efficiency deep-blue organic light-emitting diodes based on a thermally activated delayed fluorescence emitter. J. Mater. Chem. C *3*, 421–424.

Wu, C.-L., Chang, C.-H., Chang, Y.-T., Chen, C.-T., Chen, C.-T., and Su, C.-J. (2014). High efficiency non-dopant blue organic light-emitting diodes based on anthracene-based fluorophores with molecular design of charge transport and red-shifted emission. J. Mater. Chem. C *2*, 7188–7200.

Wu, T.-L., Huang, M.-J., Lin, C.-C., Huang, P.-Y., Chou, T.-Y., Chen-Cheng, R.W., Liu, H.-W., Liu, R.-S., and Cheng, C.-H. (2018). Diboron compound-based organic light-emitting diodes with high efficiency and reduced efficiency roll-off. Nat. Photon. *12*, 235–240.

Young, R.H., Tang, C.W., and Marchetti, A.P. (2002). Current-induced fluorescence quenching in organic light-emitting diodes. Appl. Phys. Lett. *80*, 874–876.

Zambianchi, M., Benvenuti, E., Bettini, C., Zanardi, C., Seeber, R., Gentili, D., Muccini, M., Biondo, V., Soldano, C., Generali, G., et al. (2016). Anthracene-based molecular emitters for non-doped deep-blue organic light emitting transistors. J. Mater. Chem. C *4*, 9411–9417.

Zhang, Q., Li, B., Huang, S., Nomura, H., Tanaka, H., and Adachi, C. (2014). Efficient blue organic light-emitting diodes employing thermally activated delayed fluorescence. Nat. Photon. *8*, 326–332.

Zhang, J., Ding, D., Wei, Y., Han, F., Xu, H., and Huang, W. (2016). Multiphosphine-oxide hosts for ultralow-voltage-driven true-blue thermally activated delayed fluorescence diodes with external quantum efficiency beyond 20%. Adv. Mater. *28*, 479–485.

Zhang, Z., Du, J., Zhang, D., Sun, H., Yin, L., Ma, L., Chen, J., Ma, D., Cheng, H., and Ren, W. (2017). Rosin-enabled ultraclean and damage-free transfer of graphene for large-area flexible organic light-emitting diodes. Nat. Commun. *8*, 14560.

ISCI, Volume *9*

Supplemental Information

Efficient Deep-Blue Electrofluorescence with an External Quantum Efficiency Beyond 10%

Shuanglong Wang, Mengya Qiao, Zhonghua Ye, Dehai Dou, Minyu Chen, Yan Peng, Ying Shi, Xuyong Yang, Lei Cui, Jiuyan Li, Chunju Li, Bin Wei, and Wai-Yeung Wong

Supplemental information

Efficient Deep-blue Electrofluorescence with an External Quantum Efficiency Beyond 10%

Shuanglong Wang,[1,6] Mengya Qiao,[2,6] Zhonghua Ye,[3] Dehai Dou,[1] Minyu Chen,[1] Yan Peng,[1] Ying Shi,[3] Xuyong Yang,[1] Lei Cui,[2] Jiuyan Li,[4] Chunju Li,[2,*] Bin Wei,[1,*] Wai-Yeung Wong[5,7,*]

[1]School of Mechatronic Engineering and Automation, Key Laboratory of Advanced Display and System Applications, Ministry of Education, Shanghai University, 149 Yanchang Road, Shanghai, 200072, P. R. China.

[2]Department of Chemistry, Center for Supramolecular Chemistry and Catalysis, Shanghai University, Shanghai 200444, P. R. China.

[3]School of Materials Science and Engineering, Shanghai University, Shanghai 200444, P. R. China.

[4]School of Chemical Engineering, Dalian University of Technology, Liaoning, 116024, P. R. China

[5]Institute of Molecular Functional Materials and Department of Applied Biology and Chemical Technology, Hong Kong Polytechnic University, Hung Hom, Kowloon, Hong Kong, P. R. China

[6]These authors equally contributed to this work.

[7]Lead Contact

*Correspondence: cjli@shu.edu.cn (C.J.L)
bwei@shu.edu.cn (B.W)
wai-yeung.wong@polyu.edu.hk (W.-Y.W)

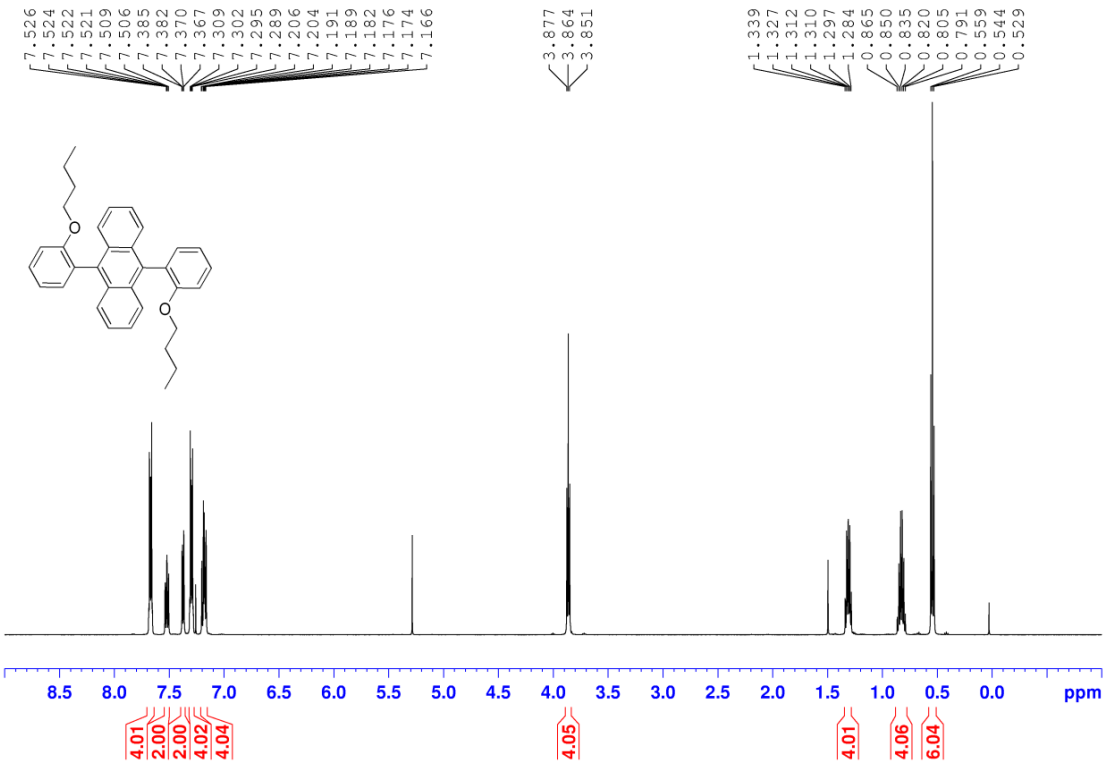

Figure S1. ^{1}H NMR spectrum of (500 MHz) of BBPA in $CDCl_3$. Related to Figure 1.

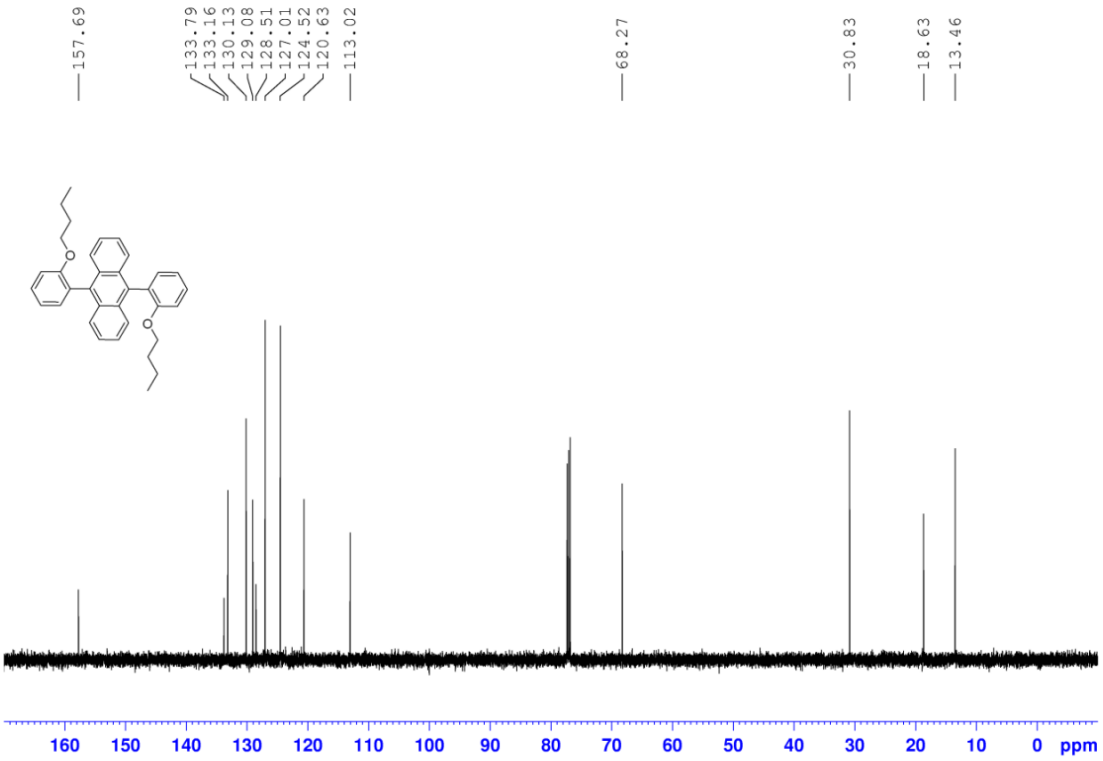

Figure S2. ^{13}C NMR spectrum of (125 MHz) of BBPA in $CDCl_3$. Related to Figure 1.

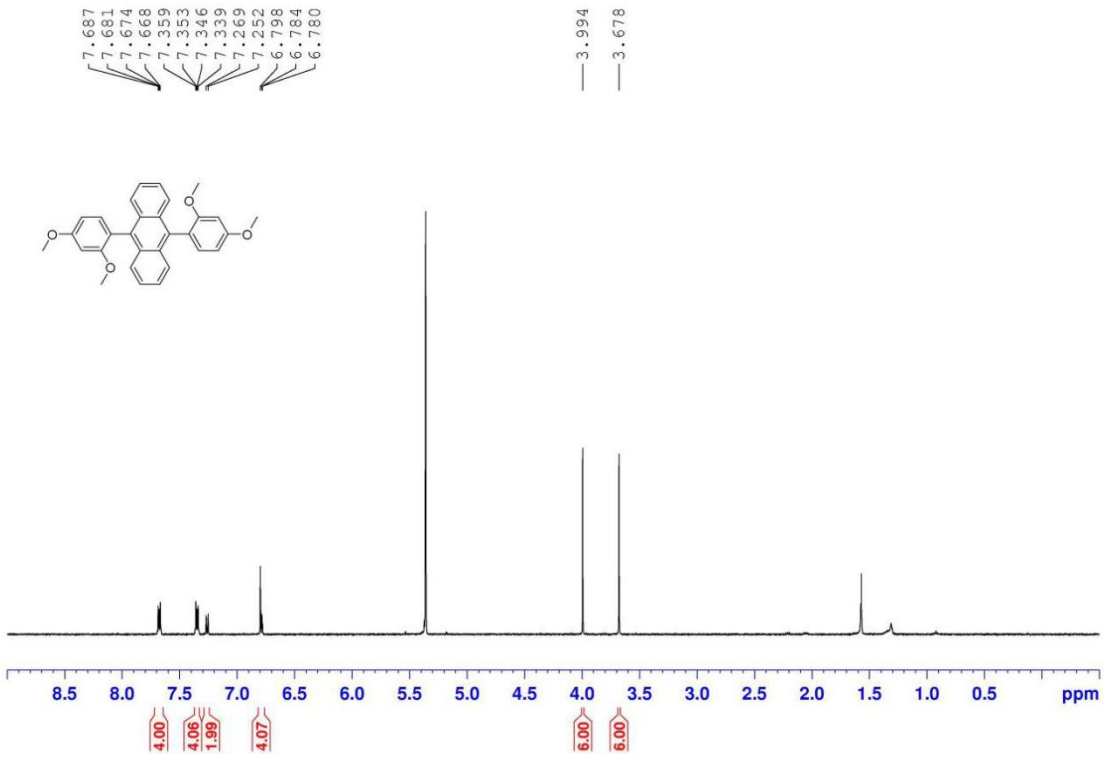

Figure S3. ^{1}H NMR spectrum of (500 MHz) of DMPA in CD_2Cl_2. Related to Figure 1.

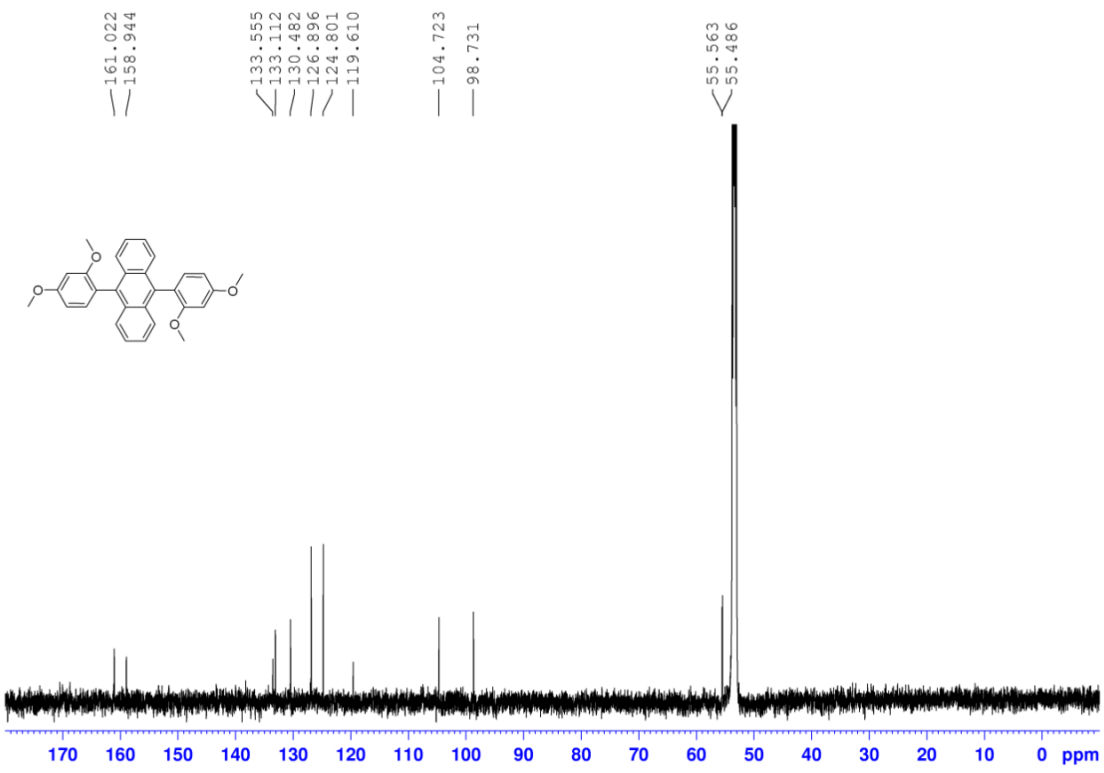

Figure S4. ^{13}C NMR spectrum of (150 MHz) of DMPA in CD_2Cl_2. Related to Figure 1.

Table S1. Crystal data and structure refinement for BBPA. Related to Figure 1 and Data S1

Compound	BBPA	
Empirical formula	$C_{34}H_{34}O_2$	
Formula weight	474.61	
Temperature	203(2) K	
Wavelength	0.71073 Å	
Crystal system	Triclinic	
Space group	*P*-1	
Unit cell dimensions	a = 7.9384(17) Å	α= 102.876(3)°
	b = 9.3043(19) Å	β= 105.317(3)°
	c = 9.5439(19) Å	γ= 101.627(3)°
Volume	636.9(2) $Å^3$	
Z	1	
Density (calculated)	1.237 Mg/m^3	
Absorption coefficient	0.075 mm^{-1}	
F(000)	254	
Crystal size	0.400 x 0.300 x 0.200 mm^3	
Theta range for data collection	2.314 to 27.000°.	
Index ranges	-10<=h<=9, -10<=k<=11, -12<=l<=11	
Reflections collected	4508	
Independent reflections	2733 [R(int) = 0.0189]	
Completeness to theta = 25.242°	98.4 %	
Absorption correction	Semi-empirical from equivalents	
Max. and min. transmission	0.970 and 0.785	
Refinement method	Full-matrix least-squares on F^2	
Data / restraints / parameters	2733 / 0 / 164	
Goodness-of-fit on F^2	1.085	
Final R indices [I>2sigma(I)]	R1 = 0.0449, wR2 = 0.1278	
R indices (all data)	R1 = 0.0582, wR2 = 0.1540	
Largest diff. peak and hole	0.241 and -0.237 $e.Å^{-3}$	

Table S2. The energies of the highest occupied molecular orbital (HOMO) and lowest unoccupied molecular orbital (LUMO) are calculated using the B31PY/6-31 G(d) level of theory. Related to Figure 1.

Emitter	HOMO (eV)	LUMO (eV)	Energy Gap (eV)
BBPA	-4.87	-1.37	3.50
DMPA	-4.86	-1.41	3.45

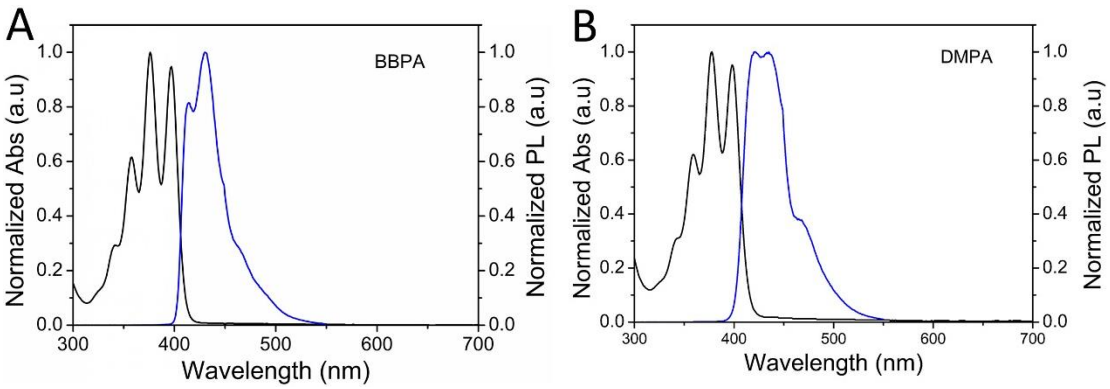

Figure S5. UV-vis absorption (black line) and PL spectra (blue line) of (**A**) BBPA and (**B**) DMPA in CH_2Cl_2 (10^{-5} M), respectively. Related to Figure 2 and Table 1.

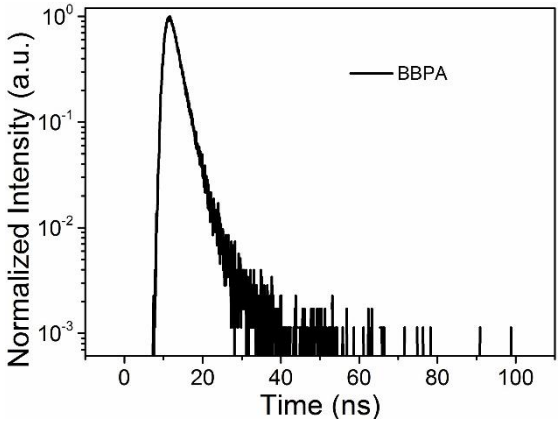

Figure S6. The corresponding PL decay spectra of BBPA in solid film at ambient condition. Related to Figure 2.

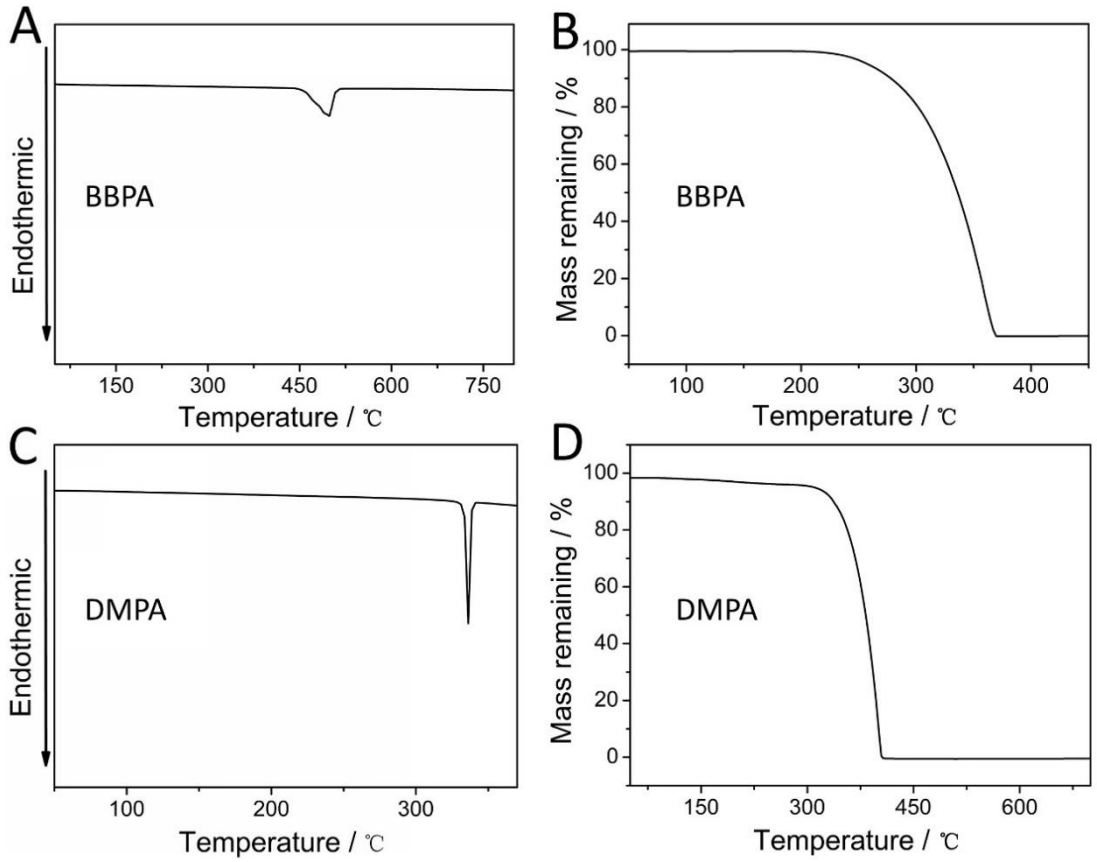

Figure S7. Thermal gravimetric analysis (TGA) of BBPA (**A**) and DMPA (**C**) and differential scanning calorimetry (DSC) analysis of BBPA (**B**) and DMPA (**D**), respectively. Related to Figure 2 and Table 1.

Photoelectron yield spectroscopy in the air (AC-3, IPS-3Riken Keiki) was conducted to determine the HOMO energy level of the materials. The HOMO energy level was obtained from the intersection point of the ground level with the approximate line of the square of photon counts per second.

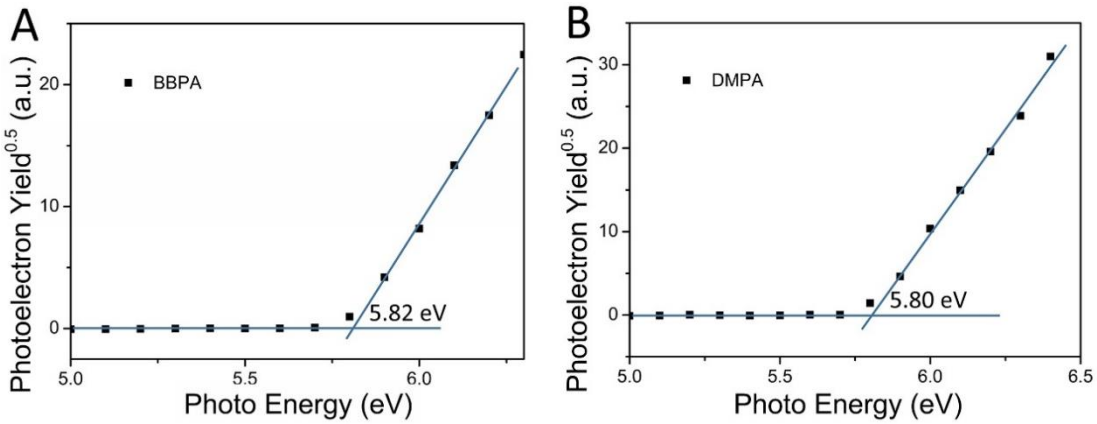

Figure S8. The squares of the photoelectron yield measured in air atmosphere plotted as a function of the photon energy for (**A**) BBPA and (**B**) DMPA. Ionization

potentials are determined from the onset of the plots. Related to Table 1.

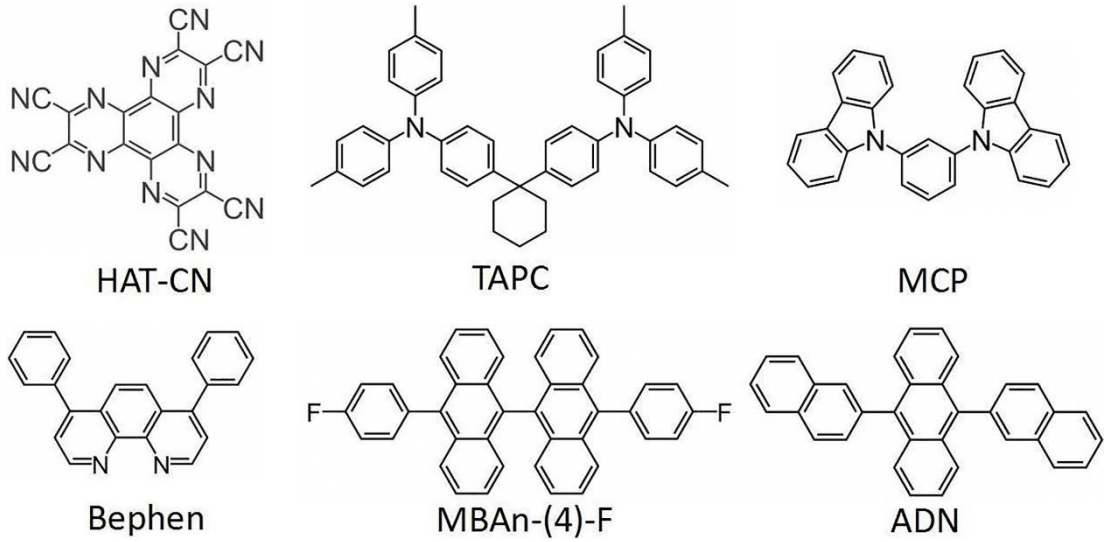

Figure S9. **Chemical structures of the materials described in the OLED devices.** Related to Figure 3.

We explored the PL spectra of non-doped film and blend film (TAPC:50% dopants) for BBPA and DMPA, respectively. The performance characteristics of these films are shown in Figure S10. The exciplex emission of the TAPC:50% BBPA and TAPC:50% DMPA emitter were not observed at 500-700 nm. The results implied that the peak emissions within 500-700 nm are not originated from exciplex emission between TAPC and EML. In addition, we also fabricated non-doped devices employing PEDOT:PSS as the hole transporting layer to prove that emission peak at 500 nm arises from the excimer of BBPA and DMPA based on the structure of ITO/PEDOT:PSS/EML/Bephen/Liq/Al. Figure S11 shows the EL spectra of nondoped BBPA and DMPA based devices. The EL spectra based on solution-processed devices also showed an emission peak. These results also proved that the emission peak within 500-700 nm is originated from the excimer of BBPA and DMPA, respectively.

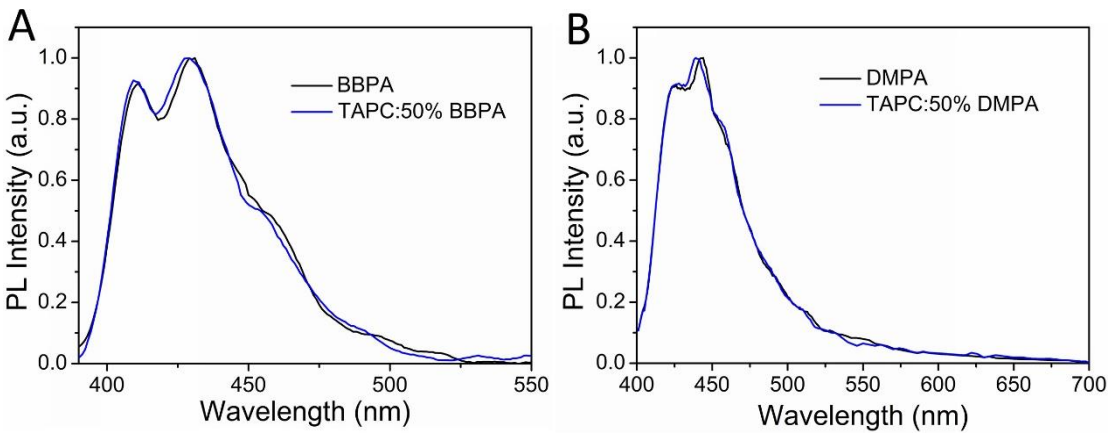

Figure S10. Comparison of the emission (PL) spectra of (**A**) BBPA and (**B**) DMPA in the neat films (black) and doped films (TAPC:50% dopants) (blue), respectively. Related to Figure 4.

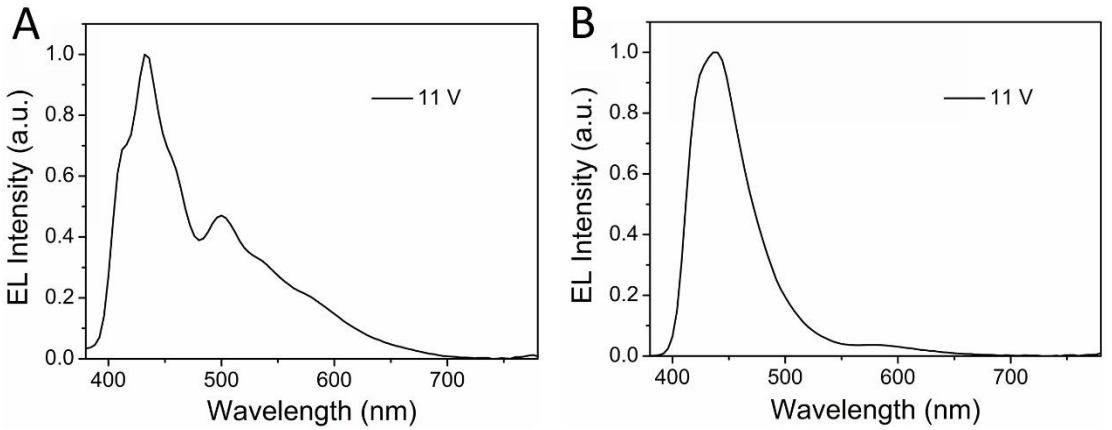

Figure S11. EL spectra of BBPA (**A**) and DMPA film (**B**) based solution-processed devices. Related to Figure 4.

We have optimized doped EL device of A1 and B1 and tuned the doping concentration using mCP as the host with the identical device structure. The doping levels are 3%, 5% and 10%. Relevant EL data about device A1 can be seen in Figure S12 and Table S3. The configuration of the different kinds of doped devices is shown below:

Device A1-1: ITO/HAT-CN (5 nm)/TAPC (40 nm)/mCP:3% BBPA (20 nm)/Bphen (30 nm)/Liq (1 nm)/Al (150 nm).

Device A1-2: ITO/HAT-CN (5 nm)/TAPC (40 nm)/mCP:10% BBPA (20 nm)/Bphen (30 nm)/Liq (1 nm)/Al (150 nm).

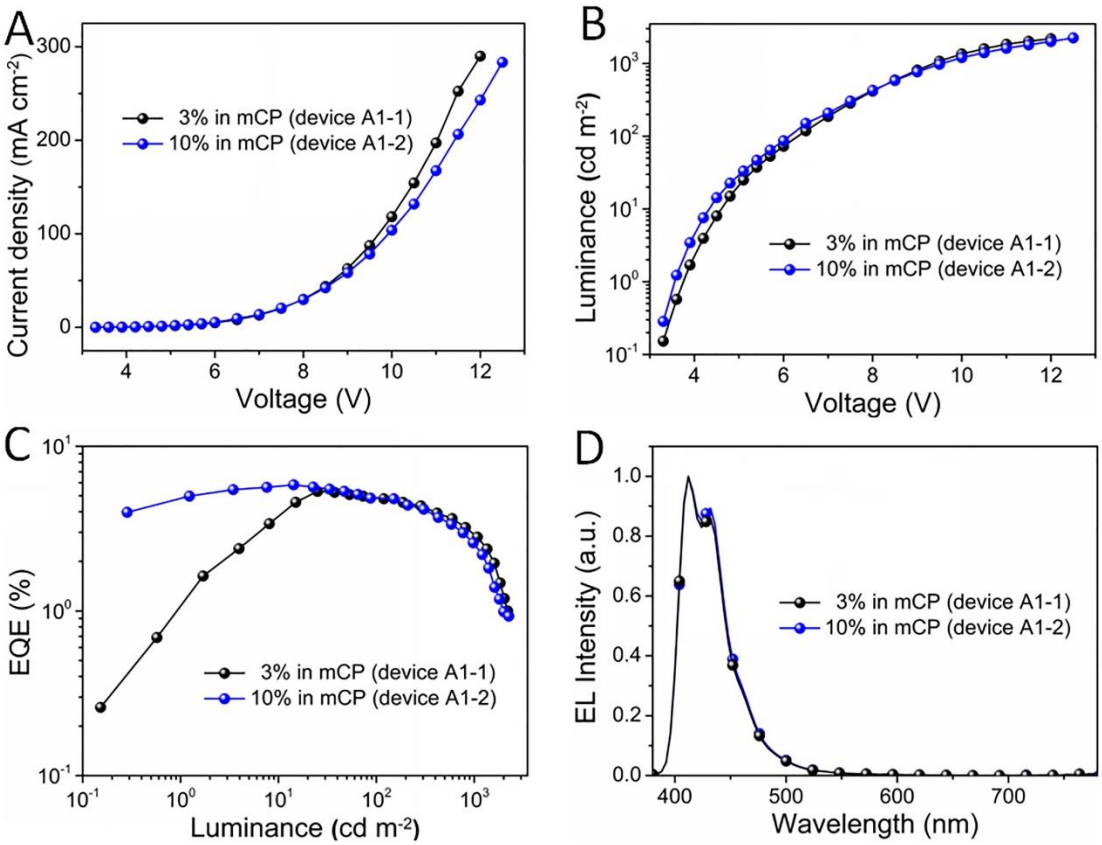

Figure S12. Performance of optimized deep blue OLEDs based on BBPA. (**A**), Current density versus voltage characteristics. (**B**), Luminance versus voltage characteristics. (**C**), External quantum efficiency versus luminance. (**D**), Electroluminescent spectra. Related to Figure 4.

Table S3. Summary of OLED characteristics of devices A1-1 and A1-2. Related to Figure 4.

Device	Emitter	V_{on}[a]	EL[b]$_{max}$	CIE[c][x, y]	FWHM[d][nm]	EQE[e][%]
A1-1	mCP:3% BBPA	3.7	412	0.15, 0.03	43	5.32
A1-2	mCP:10% BBPA	3.5	412	0.15, 0.03	43	5.83

[a]The operating voltage at a brightness of 1 cd/m^2. [b]The EL emission wavelength at the maximum intensity. [c]CIE 1931 coordinates at 7 V. [d]FWHM of EL. [e]EQE at the maximum value.

The dopant level was also optimized for device B1 (3, 5, and 10 wt% of DMPA in mCP) and the performance characteristics are shown in Figure S13.

Device B1-1: ITO/HAT-CN(5 nm)/TAPC(40 nm)/mCP:3wt% DMPA(20 nm)/Bphen (30 nm)/ Liq (1 nm)/Al(100 nm)

Device B1-2: ITO/HAT-CN(5 nm)/TAPC(40 nm)/mCP:10wt% DMPA(20 nm)/Bphen

(30 nm)/ Liq (1 nm)/Al(100 nm)

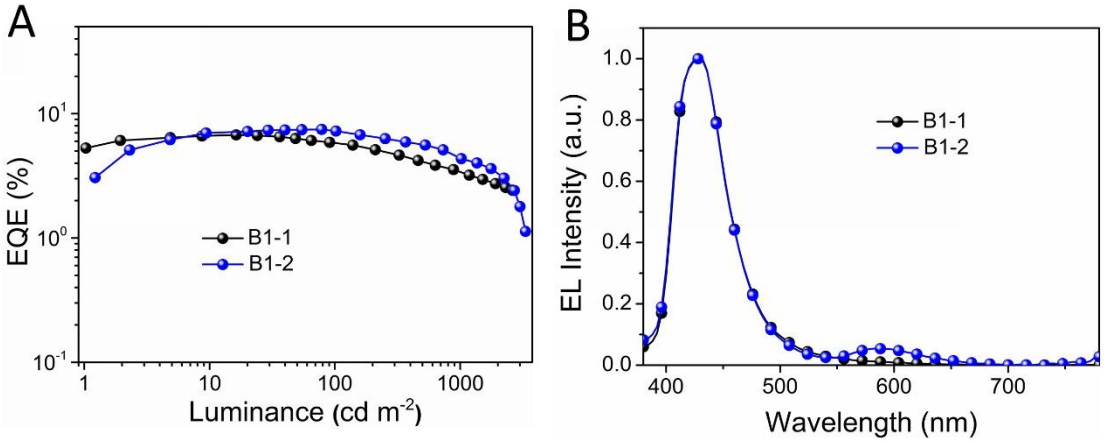

Figure S13. Performance of optimized deep blue OLEDs based on DMPA. (**A**), External quantum efficiency versus luminance. (**B**), Electroluminescent spectra. Related to Figure 4 and Table 2.

To understand the charge balance of the emitting layer from these OLEDs, we fabricated hole-only and electron-only devices of devices B1 and A2. The performance characteristics of these charge-only devices are shown in Figure S14.

Device B1: ITO/HAT-CN (5 nm)/TAPC (40 nm)/mCP:DMPA (5%) (20 nm)/NPB (5 nm)/Al (100 nm) for hole-only devices, ITO/Bphen (20 nm)/mCP:DMPA (5%) (20 nm)/Bphen (30 nm)/Liq (1 nm)/Al (100 nm) for electron-only devices

Device A2: ITO/HAT-CN (5 nm)/TAPC (40 nm)/ADN:BBPA (5%) (20 nm)/NPB (5 nm)/Al (100 nm) for hole-only devices, ITO/Bphen (20 nm)/ ADN:BBPA (5%) (20 nm)/Bphen (30 nm)/Liq (1 nm)/Al (100 nm) for electron-only devices

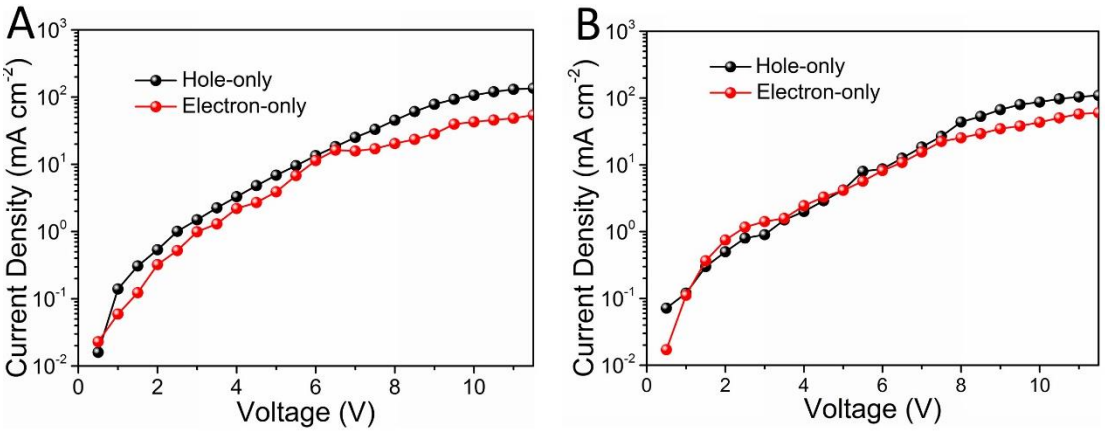

Figure S14. Performance of hole-only and electron-only devices based on device B1 (**A**) and A2 (**B**). Related to Figure 5.

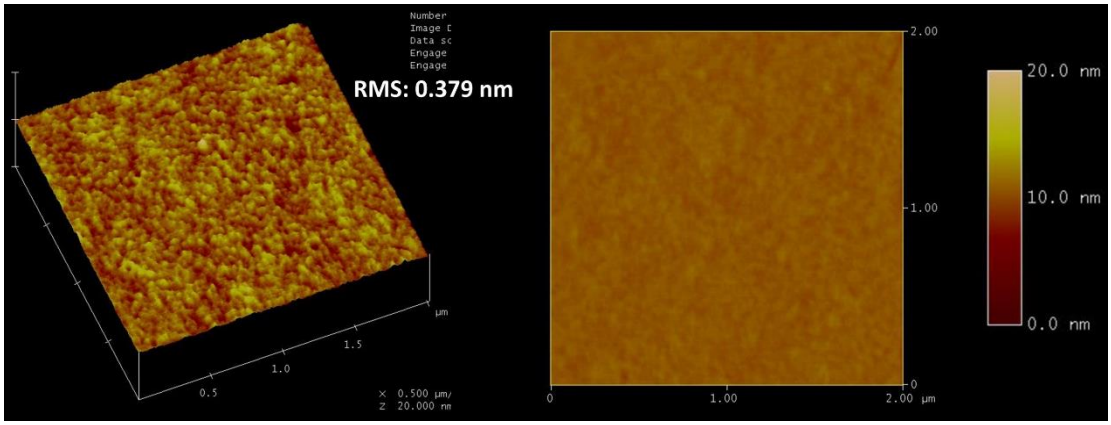

Figure S15. AFM topographic images of MBAn-(4)-F:5% BBPA by vacuum-deposition in thin solid films. Related to Figure 5.

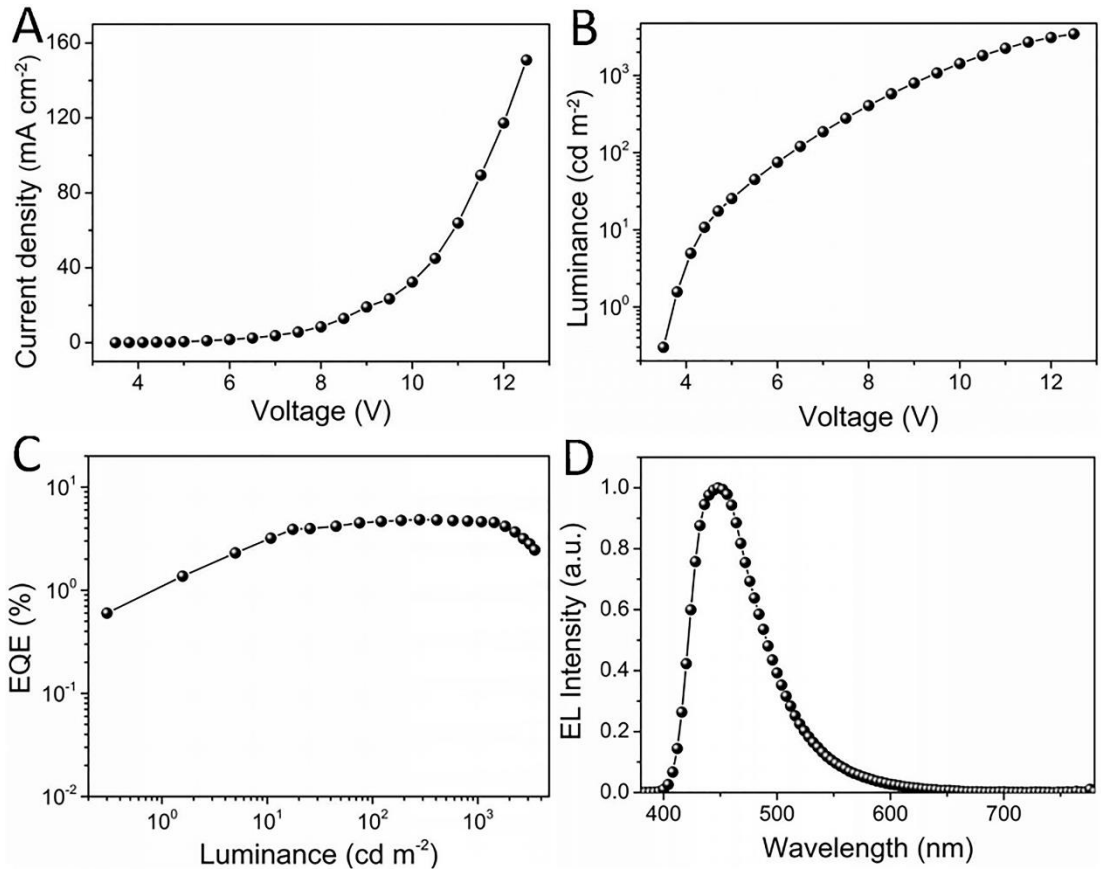

Figure S16. Performance of ADN:5% DMPA based OLEDs (device B2). (**A**), Current density versus voltage characteristics. (**B**), Luminance versus voltage characteristics. (**C**), External quantum efficiency versus luminance. (**D**), Electroluminescent spectra. Related to Figure 5 and Table 2

Table S4. Summary of performance characteristics based on device B3. Related to Figure 5 and Table 2.

Device[a]	Emitter	V_{on}[b] [V]	EL[c][λ_{max}]	CIE[d][x, y]	FWHM[e][nm]	EQE_{max}(%)
B3	MBAn-(4)-F:DMPA	3.8	440	0.15, 0.06	50	5.68

[a]Device configuration: ITO/HAT-CN(5 nm)/TAPC(40 nm)/EML(20 nm)/Bphen (30 nm)/Liq(1 nm)/Al(100 nm). [b]The operating voltage at a brightness of 1 cd/m^2. [c]The EL emission wavelength at the maximum intensity. [d]CIE 1931 coordinates at 7 V. [e]FWHM of EL spectra.

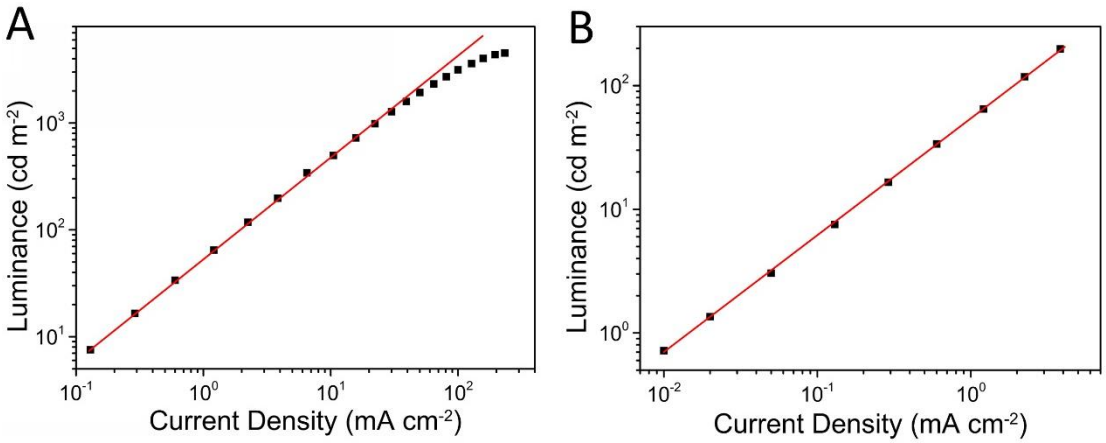

Figure S17. Dependence of the luminance of the device employing MBAn-(4)-F:5% BBPA layer on the current density. (**A**) High injection current density. (**B**) Low injection current density. Related to Figure 5.

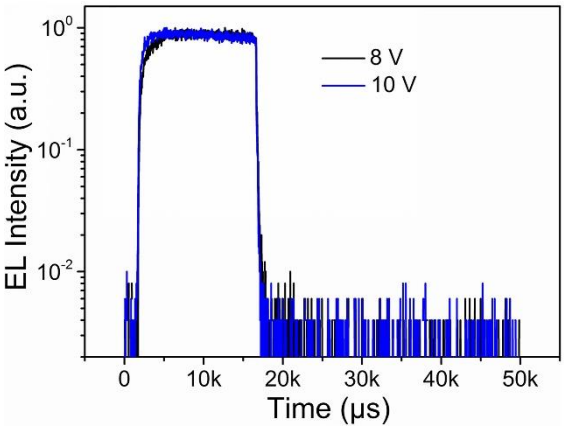

Figure S18. Transient EL decay of device A3 using MBAn-(4)-F:5% BBPA emitter. Related to Figure 5.

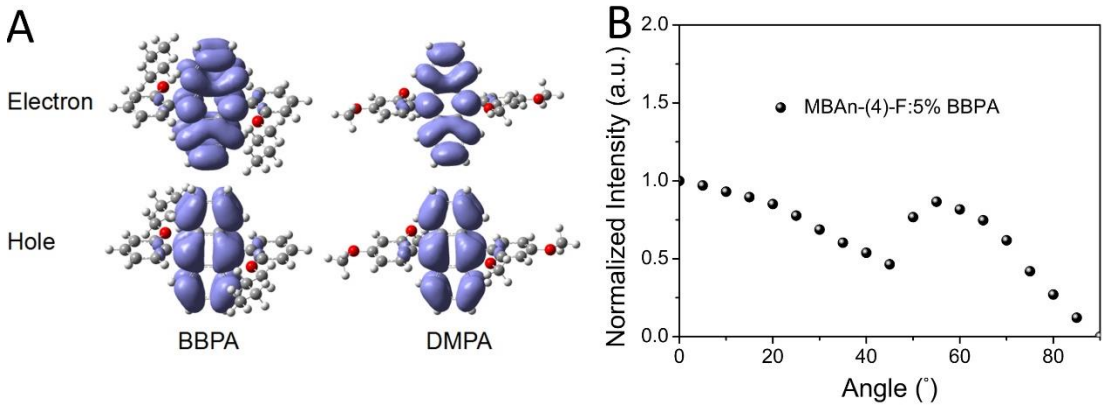

Figure S19. (**A**), NTO analysis of BBPA and DMPA (**B**), Measured results of PL intensity of the films with 5 wt% BBPA compound doped into MBAn-(4)-F at different angles. Related to Figure 5.

Transparent Methods

General information

All chemicals and reagents in this work were used as received from commercial sources without purification unless otherwise stated. MBAn-(4)-F was synthesized in our previous work (Wei et al., 2017). The other organic functional molecules were obtained from e-Ray Optoelectronics Corp. (Taipei, Taiwan). Indium tin oxide (ITO, 15 Ω per sheet, 150 nm)-coated glass substrates were ordered from CSG Holding Co. Ltd (China).

Synthesis of materials

trans-9,10-Bis(2-butoxyphenyl)anthracene

9,10-Dibromoanthracene (0.67 g, 2.0 mmol), 2-butoxyphenylboronic acid (0.78 g, 4.0 mmol), and Na_2CO_3 (0.88 g, 8.0 mmol) were dissolved in a mixed solvent of 1.4-dioxane (40 mL) and water (10 mL). Tetrakis-(triphenylphosphine)palladium (0.12 g, 0.10 mmol) was then added and the solution was heated to reflux with stirring for 24 h. The solvent was evaporated under vacuum, and the mixture was extracted with ethyl acetate (20 mL) and washed with brine (15 mL) and water (15 mL). The organic layer was dried over anhydrous sodium sulfate and then concentrated. The residue was purified by column chromatography on silica gel (eluent: 1:40 v/v CH_2Cl_2/petroleum ether) to afford 9,10-bis(2-butoxyphenyl) anthracene (0.26 g, 27%) as a white solid. ^{1}H NMR (500 MHz, $CDCl_3$): δ (ppm): 7.69-7.67 (m, 4H), 7.53 (td, J_1 = 7.89 Hz, J_2 = 1.73 Hz, 2H), 7.39 (dd, J_1 = 7.29 Hz, J_2 = 1.72 Hz, 2H), 7.32-7.30 (m,

4H), 7.21-7.17 (m, 4H), 3.87 (t, *J* = 6.47 Hz, 4H), 1.30-1.35 (m, 4H), 0.87-0.80 (m, 4H), 0.56 (t, *J* = 7.42 Hz, 6H). ^{13}C NMR (125 MHz, $CDCl_3$): δ (ppm): 157.7, 133.8, 133.2, 130.1, 129.1, 128.5, 127.0, 124.5, 120.6, 113.0, 68.3, 30.8, 18.6, 13.5, HRMS (ESI): $[C_{34}H_{34}O_2+H]$+. calcd *m/z* 475.2632; found *m/z* 475.2647.

trans-9,10-Bis-(2,4-dimethoxyphenyl)-anthracene

9,10-Dibromoanthracene (0.67 g, 2.0 mmol), 2,4-dimethoxybenzeneboronic acid (1.46 g, 8.0 mmol), and Na_2CO_3 (1.3 g, 12 mmol) were dissolved in a mixed solvent of 1.4-dioxane (40 mL) and water (10 mL). Tetrakis-(triphenylphosphine)palladium (0.12 g, 0.10 mmol) was then added and the solution was heated to reflux with stirring for 24 h. The solvent was evaporated under vacuum, and the mixture was extracted with dichloromethane (20 mL) and washed with brine (15 mL) and water (15 mL). The organic layer was dried over anhydrous sodium sulfate and then concentrated. The residue was purified by column chromatography on silica gel (eluent: 1:1 v/v CH_2Cl_2/petroleum ether) to afford *trans*-9,10-bis- (2,4-dimethoxyphenyl)anthracene (0.31 g, 34%) as a white solid. ^{1}H NMR (500 MHz, CD_2Cl_2): δ (ppm): 7.69-7.66 (m, 4H), 7.37-7.33 (m, 4H), 7.26 (d, *J*=7.31 Hz, 2H), 6.80-6.77 (m, 4H), 3.99 (s, 6H,), 3.68 (s, 6H). ^{13}C NMR (150 MHz, CD_2Cl_2): δ (ppm): 161.0, 158.9, 133.6, 133.1, 130.5, 126.9, 124.8, 119.6, 104.7, 98.7, 55.6, 55.5. HRMS (ESI): $[C_{30}H_{26}O_4+H]$+, calcd *m/z* 451.1904; found *m/z* 451.1915.

Measurements

^{1}H NMR and ^{13}C NMR spectra were measured with a Bruker Avance 500 MHz instrument in $CDCl_3$ or CD_2Cl_2. High-resolution mass spectra (HRMS) were recorded on a Bruker Daltonics, Inc. APEXIII 7.0 TESLA FTMS instrument. UV-vis absorption spectra were recorded on a UV-2501PC spectrophotometer at room temperature. Photoluminescent spectra of these complexes were tested on an Edinburgh Instruments Ltd (FLSP920) fluorescence spectrophotometer in the solid state. The transient EL decay spectra were tested using a transient spectrometer (Edinburg FL920P). The PLQYs were determined with an integrating sphere at room temperature. Photoelectron spectroscopy (PES) measurements in air were conducted using on an AC-2 (IPS-3) photoelectron spectrometer (Riken-Keiki Co.). Thermal analysis was performed using a Pegasus Q500 TGA (NETZSCH,TGA 209) thermo gravimetric analyzer under a nitrogen atmosphere at a heating rate of 10 ℃/min. Differential scanning calorimetry (DSC) was conducted under nitrogen using a

Chimaera instrument Q100 DSC (NETZSCH,DSC 200). The sample was heated at 10 ℃ min from 30 ℃ to 800 ℃.

Device fabrication

Devices were fabricated by vacuum evaporation in the structure of ITO/HAT-CN (5 nm)/TAPC (40 nm)/mCP:dopants (20 nm)/Bphen (30 nm)/Liq(1 nm)/Al (150 nm) under a base pressure lower than 1.0×10^{-5} mbar, where ITO (indium tin oxide) is the anode, 4,5,8,9,11-hexaazatriphenylenehexacabonitrile (HAT-CN) is the hole injection layer; (di-(4-(N,N-ditolylamino)phenyl)cyclohexane) (TAPC) is the hole transporting layer; 1,3-bis(N-carbazolyl)benzene (mCP) is the blue host material; 4,7-diphenyl-1,10-phenanthroline (Bphen) is the electron transporting layer, 8-hydroxyquinolinato lithium (Liq) and Al are electron injection layer and cathode, respectively. ITO coated glass was used as the substrate and the sheet resistance was 15 Ω sq^{-1}. Prepared ITO glass substrates were cleaned using detergent, de-ionized water, acetone, and isopropanol. Immediately prior to loading into a custom-made high vacuum thermal evaporation chamber, the substrates were treated with a UV-ozone environment for 20 mins. Then, organic layers and a metal cathode layer were evaporated successively by using shadow masks. The entire organic layers and the Al cathode were deposited without exposure to the atmosphere, by which OLEDs with an active areas of 4 mm^2 were obtained. The deposition rates for the organic materials, and Al were typically 1.0 and 5.0 Å s^{-1}, respectively.

Device characterization

The EL characteristics were measured using a Keithley 2400 source meter and a PR650 Spectra Colorimeter under ambient condition at room temperature. The luminance and spectra of each device were measured in the direction perpendicular to the substrate.

Supplemental References

Si, C.F., Li, Z., Guo, K.P., Lv, X., Pan, S.H., Chen, G., and Wei, B. (2017). Functional versatile bipolar 3,3′-dimethyl-9,9′-bianthracene derivatives as an efficient host and deep-blue emitter. Dyes Pigments *148*, 329-340.